Self-induced marginality in plastically deformed crystals

O. U. Salman [1,2], A. Ahadi [2] and L. Truskinovsky [3]
[1] *LSPM, CNRS UPR3407, Université Sorbonne Paris Nord, 93400 Villateneuse, France*
[2] *Department of Industrial and Mechanical Sciences, Lund University, SE-221 00 Lund, Sweden*
[3] *PMMH, CNRS UMR 7636 ESPCI PSL, 10 Rue Vauquelin, 75005 Paris, France*

(Received 11 November 2025; accepted 23 September 2026; published 30 October 2026)

Quasibrittle plastic yielding is a salient feature of well-annealed glassy materials. We show that a similar mechanical response is characteristic of perfect crystals after they experience mechanically-induced massive nucleation of dislocations. We argue that such 'preparation' effectively converts a mechanically crystalline sample into a mechanically pseudoamorphous one. To understand the nature of the associated transformation we study a model 2D crystal subjected to AQS driving. We show that pristine crystals 'primed' in this way exhibit both pre- and postyield dislocation avalanches with power-law statistics. The value of the computed exponents is indicative of self-induced marginal stability. Our main tool is the novel mesoscopic tensorial model (MTM) of crystal plasticity representing a conceptual trade-off between continuum and atomic descriptions. It captures the specificity of crystals with different lattice symmetry at relatively low computational cost while relying minimally on phenomenology. Rather strikingly, MTM allows one to deal with a statistically meaningful number of dislocations while accounting in a geometrically exact way for finite deformations. The obtained results challenge the prevailing opinion that crystal and amorphous plasticity are fundamentally different phenomena. As MTM does not deal with dislocations directly, our work reinforces the idea that in both cases it is the elastic incompatibility which evolves through intermittent avalanches.

DOI: 10.1103/3rwf-d3yx

I. INTRODUCTION

The complexity of plastic response of strain-driven crystalline solids is revealed by intermittent stress fluctuations accompanied by scale-free spatial organization of dislocations [1–10]. The same general features are also typical of amorphous plasticity [11–20]. To build a conceptual link between the two phenomena, we study in this paper a relatively transparent prototypical model of a 2D square crystal subjected to athermal quasistatic (AQS) proportional loading by shear strain applied along one of the slip directions.

An important question is how to make sure that we perform numerical experiments with a realistic crystal which necessarily contains a certain amount of dislocations. To prepare a 'generic' crystal we start from a pristine dislocation-free crystal and shear it to the limit of its mechanical stability. The associated spinodal instability is resolved through massive nucleation of dislocations. We argue that such 'preparation' effectively converts a mechanically crystalline sample into a mechanically pseudoamorphous one [21–23]. We use this term vaguely to refer to a solid that is structurally crystalline while exhibiting quasiamorphous mechanical response. The amorphous component of such a response reveals itself through various nonaffine relaxations under homogeneous loading but, most importantly, through characteristic statistics of fluctuations indicative of mechanical marginality of the system [24,25].

Specifically, we show that the plastic response of our pseudoamorphous crystals begins with a hardening stage involving small spatially localized dislocations rearrangements. Such 'microplasticity' regime is terminated abruptly with a quasibrittle transition to the full scale plastic yield. During such transition we observe the formation of multigrain pattern dominated by global structures reminiscent of shear bands. The postyield regime is characterized by a stress plateau with superimposed fluctuations. The latter represent broadly distributed dislocation avalanches with power-law statistics. Similar quasibrittle yield has been observed in well-annealed glasses [26–34]. To make sense of the observed similarity of mechanical responses, we argue that despite the absence of dislocations in amorphous plasticity, both amorphous and crystalline plasticity can be viewed as representing an evolution of elastic incompatibility. In particular, in both cases the underlying elementary mechanical events can be represented by standard shear eigenstrains [35–42].

We study the implied correlated dynamics of a large number of dislocations using the simplest mesoscopic model of a crystal loaded by shear strain applied along one of the slip directions. Specifically, we use the mesoscopic tensorial model (MTM) representing a conceptual trade-off between continuum and atomic descriptions of crystal plasticity [43–50]. An important advantage of the MTM is that it accounts for micromechanisms of plastic response while relying minimally

Published by the American Physical Society under the terms of the Creative Commons Attribution 4.0 International license. Further distribution of this work must maintain attribution to the author(s) and the published article's title, journal citation, and DOI. Funded by Bibsam.

on phenomenology. In particular, it allows one to capture the intermittent nature of dislocation avalanches while resolving topological (connectivity) restructuring involved in nucleation and annihilation of dislocations [51]. Crucially, in contrast with other computational approaches to microscale plasticity, e.g., [52–77], the MTM allows one to deal with a statistically meaningful number of dislocations while accounting in a geometrically exact way for finite deformations [78–81].

The main idea of the MTM is to associate with material elements an effective energy landscape whose tensorial periodicity accounts for crystallographically invariant deformations. The resulting Landau-type model is characterized by infinitely many equivalent energy wells [43–50,82–92] with plastically deformed crystal emerging as a multiphase mixture. Strikingly, dislocations play in the MTM the role of domain boundaries. The small scale regularization is achieved by mesoscopic discretization reminiscent of what is done in large eddy simulations of fluid turbulence.

Despite operating with engineering concepts of stress and strain, the MTM correctly captures not only long-range elastic interactions of effective mesoscale dislocations but also describes adequately their short-range interactions. This eliminates the need for 'local rules' describing nucleation and annihilation of dislocations and, more generally, opens the way to phenomenology-free description of the formation of complex dislocational entanglements.

The 2D version of the MTM, used in our numerical experiments, has some formal similarity with a single-slip-plane phase field model of Peierls-Nabarro type, which was also found adequate to represent the critical nature of plastic flows, e.g., [61,93]. The main difference of our approach is the use of finite strain bulk elasticity compatible with multislip and the ability to capture adequately lattice rotations. Some precursors of the MTM approach can be found in [94–101], see also a parallel recent development in [97,102,103].

The paper is organized as follows. In Sec. II we introduce the MTM model and discuss the fine structure of the infinitely periodic energy landscape used in our numerical experiments. The numerical method is detailed in Sec. III. Our computational observations are collected in Sec. IV. The technique of extracting the critical exponents is discussed in Sec. V where we also present our main scaling results. The final Sec. VI contains our conclusions.

II. THE MODEL

Consider the continuum deformation field

$$\mathbf{y} = \mathbf{y}(\mathbf{x}), \tag{1}$$

where $\mathbf{y}$ and $\mathbf{x}$ are positions of material points in the current and reference configurations, respectively. Due to frame indifference constraint, the strain energy density φ can depend on the deformation gradient

$$\mathbf{F} = \nabla \mathbf{y} \tag{2}$$

only through the metric tensor

$$\mathbf{C} = \mathbf{F}^T \mathbf{F} \tag{3}$$

which then plays the role of a tensorial order parameter. We assume further that the implied function

$$\varphi = \varphi(\mathbf{C}) \tag{4}$$

respects the symmetry of an underlying Bravais lattice. Such symmetry is necessarily global extending beyond the conventional point group and capturing, in particular, *lattice invariant shears*. Specifically, in 2D the global symmetry assumption implies that

$$\varphi(\mathbf{C}) = \varphi(\mathbf{m}^T \mathbf{C} \mathbf{m}), \tag{5}$$

where the unimodular integer valued matrices $\mathbf{m}$ belong to the infinite discrete group

$$GL(2, \mathbb{Z}) = \{\mathbf{m},\ m_{IJ} \in \mathbb{Z},\ \det(\mathbf{m}) = \pm 1\}. \tag{6}$$

In view of the symmetry assumption (6), the configurational space of shear deformations $\det \mathbf{C} = 1$, represented by a hyperboloid in the 3D space (C_{11}, C_{22}, C_{12}), is tessellated into an infinite number of equivalent periodicity domains. In particular, if the energy density $\varphi(\mathbf{C})$ is known in one of such domains, it can be extended to the whole configurational space of tensors $\mathbf{C}$ by the symmetry.

In what follows we refer to the restriction of the periodic energy density function $\varphi(\mathbf{C})$ with tensorial symmetry $GL(2, \mathbb{Z})$ to the minimal periodicity (fundamental) domain as $\varphi_{\mathscr{D}}(\tilde{\mathbf{C}})$, where

$$\tilde{\mathbf{C}} = \mathbf{m}^T \mathbf{C} \mathbf{m} \tag{7}$$

is the projection of a general metric tensor $\mathbf{C}$ into the domain $\mathscr{D}$ and $\mathbf{m}$ is the corresponding unimodular integer valued matrix that performs the projection while ensuring that

$$\varphi(\mathbf{C}) = \varphi_{\mathscr{D}}(\tilde{\mathbf{C}}). \tag{8}$$

The configuration of the fundamental domain $\mathscr{D}$ is well known [81,89,91,104]

$$\mathscr{D} = \left\{0 < C_{11} \leqslant C_{22}, \quad 0 \leqslant C_{12} \leqslant \frac{C_{11}}{2}\right\}, \tag{9}$$

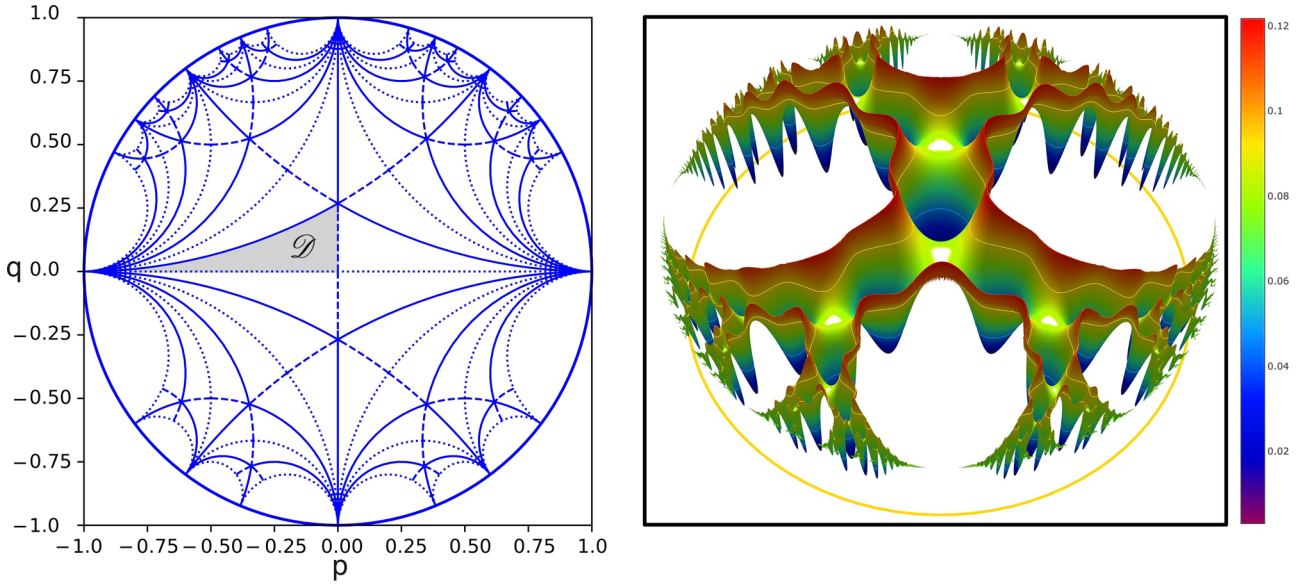
where it is implied that $\det \mathbf{C} = 1$.

Given a generic metric $\mathbf{C}$, the task of finding a unimodular matrix $\mathbf{m}$ ensuring that $\tilde{\mathbf{C}} \in \mathscr{D}$ can be formulated as a recursive algorithm which is also well known (Lagrange reduction) [91,104]. Specifically, if we define the matrices

$$\mathbf{m}_1 = \begin{pmatrix} 1 & 0 \\ 0 & -1 \end{pmatrix}, \quad \mathbf{m}_2 = \begin{pmatrix} 0 & 1 \\ 1 & 0 \end{pmatrix}, \quad \mathbf{m}_3 = \begin{pmatrix} 1 & -1 \\ 0 & 1 \end{pmatrix}, \tag{10}$$

and start with an assumption that $\mathbf{m} = \mathbb{I}$, we can proceed through the following steps: (i) If $C_{12} < 0$, change sign of C_{12} using the mapping $\mathbf{m} \to \mathbf{m}\mathbf{m}_1$; (ii) if $C_{22} < C_{11}$, swap these two components using the mapping $\mathbf{m} \to \mathbf{m}\mathbf{m}_2$; (iii) if $2C_{12} > C_{11}$, set $C_{12} = C_{12} - C_{11}$ using the mapping $\mathbf{m} \to \mathbf{m}\mathbf{m}_3$.

Note that the action of $\mathbf{m}_1$ is a reflection that ensures an acute angle between two lattice vectors of the square lattice $\mathbf{e}_i$ where $i = 1, 2$; the action of the matrix $\mathbf{m}_2$ is also a reflection as it swaps two lattice vectors $\mathbf{e}_i$. Both of these operations belong to the point group and propagate the metric only inside the corresponding 'elastic domain' (Ericksen-Pitteri neighborhood) composed of the four copies of the minimal domain $\mathscr{D}$



(a) (b)

FIG. 1. (a) $GL(2,\mathbb{Z})$-induced tessellation of the configuration space of metric tensors C_{11}, C_{22}, C_{12} with $\det \mathbf{C} = 1$ stereographically projected on the Poincaré disk $p^2 + q^2 < 1$ where $p = t(C_{11} - C_{22})/2$, $q = tC_{12}$, and $t = 2/(2 + C_{11} + C_{22})$. The highlighted domain $\mathscr{D}$ is the fundamental (minimal periodicity) domain. (b) Representative energy landscape with colors indicating the energy level. Only the lowest energy levels are visible with the bottoms of the wells corresponding to equivalent replicas of the reference square lattice.

[48,81]. Instead, the mapping defined by matrix $\mathbf{m}_3$ brings the metric outside the 'elastic domain' and therefore represents a quantized analog of the macroscopic plastic strain [47].

To visualize the implied tessellation, it is convenient to project stereographically the infinite surface $\det \mathbf{C} = 1$ on a unit (Poincaré) disk, It is depicted in Fig. 1(a), where we show in gray the fundamental (minimal periodicity) domain $\mathscr{D}$.

In our numerical experiments we used the simplest piecewise smooth function $\varphi(\mathbf{C})$ with $GL(2,\mathbb{Z})$ symmetry and minimal necessary regularity [91]. While the single-period Landau potential $\varphi_{\mathscr{D}}(\tilde{\mathbf{C}})$ could be also constructed using the classical Cauchy-Born approach, see for instance [48,49], or assumed to be piece wise quadratic [47], the authors of [91] following [87–89], represented the elastic energy density as a combination of sixth-order polynomials ensuring stress continuity over the boundaries of the periodicity domains. Specifically, they proposed to construct the function (4) as a sum of two terms:

$$\varphi_{\mathscr{D}}(\tilde{\mathbf{C}}) = \varphi_0\left(\frac{\tilde{\mathbf{C}}}{(\det \tilde{\mathbf{C}})^{1/2}}\right) + \varphi_v(\det \tilde{\mathbf{C}}), \tag{11}$$

where φ_0 accounts for contributions due to shear while φ_v penalizes volumetric deformations.

The $GL(2,\mathbb{Z})$ invariant shear term in (11) is chosen in the form [91]

$$\varphi_0\left(\frac{\tilde{\mathbf{C}}}{(\det \tilde{\mathbf{C}})^{1/2}}\right) = \beta\psi_1\left(\frac{\tilde{\mathbf{C}}}{(\det \tilde{\mathbf{C}})^{1/2}}\right) + \psi_2\left(\frac{\tilde{\mathbf{C}}}{(\det \tilde{\mathbf{C}})^{1/2}}\right). \tag{12}$$

It depends on a single parameter β allowing one to associate the ground state either with square or triangular (hexagonal) lattice.

Given the assumed order of the polynomials, the requirement of stress continuity across the whole periodic energy landscape specifies the functions ψ_1 and ψ_2

$$\psi_1 = I_1^4 I_2 - \tfrac{41}{99} I_2^3 + \tfrac{7}{66} I_1 I_2 I_3 + \tfrac{1}{1056} I_3^2, \tag{13}$$

$$\psi_2 = \tfrac{4}{11} I_2^3 + I_1^3 I_3 - \tfrac{8}{11} I_1 I_2 I_3 + \tfrac{17}{528} I_3^2, \tag{14}$$

where we introduced the hexagonal invariants of the metric tensor

$$I_1 = \tfrac{1}{3}(\tilde{C}_{11} + \tilde{C}_{22} - \tilde{C}_{12}), \tag{15}$$

$$I_2 = \tfrac{1}{4}(\tilde{C}_{11} - \tilde{C}_{22})^2 + \tfrac{1}{12}(\tilde{C}_{11} + \tilde{C}_{22} - 4\tilde{C}_{12})^2, \tag{16}$$

$$I_3 = (\tilde{C}_{11} - \tilde{C}_{22})^2(\tilde{C}_{11} + \tilde{C}_{22} - 4\tilde{C}_{12}) - \tfrac{1}{9}(\tilde{C}_{11} + \tilde{C}_{22} - 4\tilde{C}_{12})^3. \tag{17}$$

In our numerical experiments we used the value $\beta = -1/4$ which ensured that global energy minimizer is a square lattice.

The volumetric part of the energy density, which primarily influences the fine structure of the dislocation cores and also controls the formation of voids, is assumed to be of a generic form preventing infinite compression

$$\varphi_v(s) = \mu(s - \log(s)). \tag{18}$$

To keep in our numerical experiments the strain field close to the surface $\det \mathbf{C} = 1$, we adopted a sufficiently high value of the bulk modulus, $\mu = 5$.

In Fig. 1(b) we illustrate the multiwell energy landscape in the configurational space of shear strains $\mathbf{C}$ with $\det \mathbf{C} = 1$. Here the equivalent energy wells, which appear distorted due to the stereographic projection, represent the equivalent replicas of the reference square lattice. To complement Fig. 1(b)

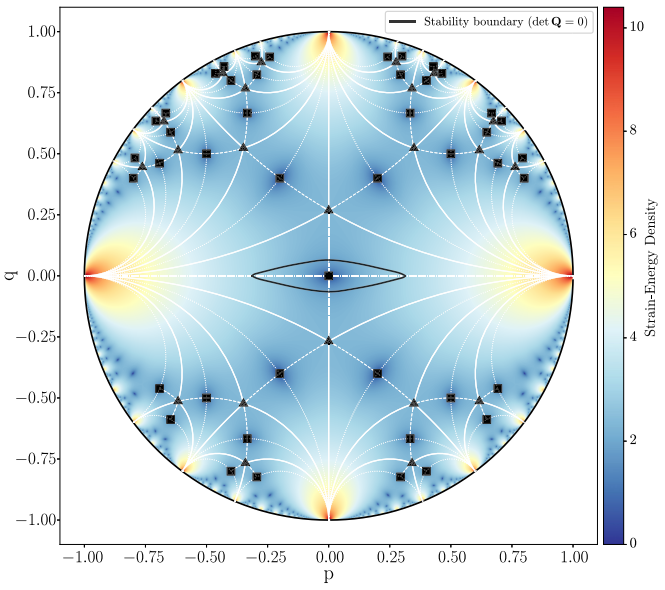


FIG. 2. Strain-energy density in the configurational space C_{11}, C_{22}, C_{12} with $\det \mathbf{C} = 1$ stereographically projected on the Poincaré disk. Thin white lines represent the $GL(2,\mathbb{Z})$ tessellation of the a Poincaré disk into equivalent periodicity domains. Colors represent energy levels following Fig. 1(b). Elastic stability boundary given by (36) is shown by the thick black contour surrounding the reference state. Small black squares and triangles correspond to equivalent square and triangular lattices, respectively.

we also show in Fig. 2, the same isochoric part of the energy landscape (Landau-type potential) but now in the level set representation. Here darker blue regions mark the neighborhoods around the bottoms of the equivalent square energy wells.

A characteristic feature of the emerging energy landscape is a network of low-energy valleys corresponding in our case to simple shears parallel to crystallographic slip planes. These valleys can be viewed as representing conventional plastic 'mechanisms'. Note that in the classical continuum crystal plasticity such valleys are effectively assumed to be flat. Instead, the MTM preserves the energy barriers separating individual wells along the low-energy valleys which is the main factor behind recurrent snap-through mechanical instabilities under quasistatic loading.

As we have seen, due to the assumed global symmetry, the emerging function $\varphi(\mathbf{C})$ is highly nonconvex. The lack of convexity of the elastic potential is a property which the MTM shares with other similar Landau-type continuum theories. The corresponding scale-free models are known to be degenerate and need to be regularized through the introduction of a cutoff length scale.

In the MTM the implied regularization is achieved through the projection of the continuum problem on a uniform mesoscale grid. In such setting the nonconvex elastic energy is associated with individual finite discrete elements. Under this assumption the infinite dimensional space of continuum deformation fields is reduced to a finite dimensional set of compatible, piecewise affine mappings. However, in contrast to the conventional finite element representation of PDEs, in the MTM the linear scale of an individual finite element h is not an irrelevant mesh size but rather a physical regularization parameter. It introduces the scale of mesoscopic elements, representing aggregates of atomic particles, and defines in this way an internal cutoff scale below which the deformation can be considered as effectively homogeneous (affine).

The choice of the value of h is then a part of the physical model. Suppose that L is the linear size of the macroscopic domain and N^2 is the number of nodes in the mesoscopic grid. Then $h = L/N$ and the corresponding dimensionless parameter is

$$\delta = h/L = 1/N. \tag{19}$$

Another dimensionless parameter in the problem is

$$\epsilon = a/L, \tag{20}$$

where a is the interatomic distance. Both ϵ and δ are small but in view of the mesoscopic nature of the MTM, we effectively assume that

$$\delta \gg \epsilon. \tag{21}$$

In the MTM approach we first implicitly perform the limit $\epsilon \to 0$ and recover in this way the continuum constitutive response of individual elements. As we have already mentioned, this can be done either by using the Cauchy-Born rule or by making a phenomenological assumption. Then, instead of performing the classical limit $\delta \to 0$ while obtaining the conventional scale-free continuum theory, the MTM operates with a small but finite value of the parameter δ.

In view of the presence of the system size L in the expression for δ one can say that the MTM effectively accounts for finite size effects. For instance, instead of saying that the size of the dislocation cores is overestimated while the number of dislocations is underestimated, one can say that the MTM deals exclusively with sufficiently small crystals. Despite this limitation, the MTM not only preserves the basic nature of long-range interaction of dislocations, but it also captures their short-range interactions, for instance, the supposedly blown up dislocations still nucleate and self-lock adequately, at least away from the boundaries of the sample.

In our numerical experiments we used the scale h obtained under the requirement that the Cauchy-Born energy density, computed for a lattice fragment with scale h, exhibits an almost periodicity within the range of strains of interest; we checked that in our case this goal is reached under the assumption that $h \sim 10a$. This would then mean that the physical size of the considered samples is of the order $L \sim 10Na$.

As we show in what follows, an incremental elastic energy minimization in the emerging discretized finite element model subjected to quasistatic loading leads to a rich repertoire of instabilities with jump discontinuities representing elastic branch switching events. The energy losses associated with such jumps contribute to plastic dissipation. While in the continuum limit such jumps merge giving rise to conventional rate-independent plasticity [105], here we maintain the discreteness of the model which is the crucial factor behind the nontrivial statistics of the emerging jump distribution.

III. NUMERICAL METHOD

We now turn to the numerical implementation of the corresponding finite dimensional elasticity problem. It reduces to finding at each value of the loading parameter the displacements of the network of discrete nodes labeled by integer-valued coordinates $a, b = 1, ..., N^2$.

In our numerical code we employ the standard linear three-node elements [106,107]. The energy of the corresponding elastic triangles undergoing affine deformation is described by the globally periodic energy landscape introduced in the previous section. The underlying assumption of globally periodic response at the mesoscopic level can be interpreted as our 'subgrid' model.

The displacement field inside each of the elements can be written in the form

$$\mathbf{u}(\mathbf{x}) = \sum_a \mathcal{N}_a(\mathbf{x}; h)\mathbf{u}_a, \tag{22}$$

where $\mathcal{N}_a(\mathbf{x}; \mathbf{h})$ are compactly supported linear shape functions and $\mathbf{u}_a$ are the nodal displacements.

Using (22) we can write the mesoscopic deformation gradient inside a single elastic element in the form

$$\mathbf{F}(\mathbf{x}; h) = \mathbb{I} + \sum_a \mathbf{u}_a \otimes \nabla\mathcal{N}_a(\mathbf{x}; h), \tag{23}$$

or in component form

$$F^i_\alpha = \delta^i_\alpha + \sum_a u^i_a \frac{\partial \mathcal{N}_a}{\partial x^\alpha}, \tag{24}$$

where i is the Eulerian index, α is the Lagrangian index, and u^i_a denotes the i-th displacement component of node a. By applying the simplest quadrature scheme we can then write the elastic energy density inside each of the elements in the form

$$w(\mathbf{x}; h) = \tfrac{1}{2}\varphi(\mathbf{C}(\mathbf{x}; h))J(\mathbf{x}, h), \tag{25}$$

where J is the Jacobian of the transformation from local dimensionless coordinates to the macroscopic reference coordinates $\mathbf{x}$. In (25) the elastic energy of a deformed triangular element $\varphi(\mathbf{C}(\mathbf{x}; h))$ depends periodically on the metric tensor whose components represent two deformed lengths of the bonds (pair interactions) and the deformed angle between them (triple interaction).

Finding a solution of the elastic problem implies parametric local minimization of the finite dimensional energy functional which we schematically write in the continuum form

$$W = \int_\Omega w(\mathbf{x}; h)d\mathbf{x}, \tag{26}$$

even though it is effectively defined on a triangular finite element network. The corresponding continuum conditions of mechanical equilibrium can be equally schematically written in the form

$$\nabla \cdot \mathbf{P} = 0, \tag{27}$$

where we introduced the first Piola-Kirchhoff stress tensor

$$\mathbf{P} = 2\mathbf{F}\mathbf{m}\boldsymbol{\Sigma}\mathbf{m}^T, \quad \text{with} \quad \boldsymbol{\Sigma} = \begin{bmatrix} \frac{\partial\varphi_{\mathscr{D}}}{\partial\tilde{C}_{11}} & \frac{1}{2}\frac{\partial\varphi_{\mathscr{D}}}{\partial\tilde{C}_{12}} \\ \frac{1}{2}\frac{\partial\varphi_{\mathscr{D}}}{\partial\tilde{C}_{12}} & \frac{\partial\varphi_{\mathscr{D}}}{\partial\tilde{C}_{22}} \end{bmatrix}. \tag{28}$$

In our discrete finite element representation the continuum equations (27) reduce to

$$\frac{\partial W}{\partial \mathbf{u}_a} = \int_\Omega \mathbf{P}(\mathbf{x}; h)\nabla\mathcal{N}_a(\mathbf{x}; h)d\mathbf{x} = 0. \tag{29}$$

In our numerical code the equations (29) are solved at each value of the loading parameter using the L-BFGS minimization algorithm [108]. It is based on constructing a positive definite approximation to the Hessian, and enabling quasi-Newton steps that progressively reduce the total energy. Iterations continue until the energy change per iteration falls below a prescribed tolerance.

More specifically, at each iteration, starting from an approximate solution $\mathbf{w}_a$, we compute a displacement correction

$$\Delta\mathbf{w}_a = \mathbf{u}_a - \mathbf{w}_a \tag{30}$$

by solving the linearized equations of equilibrium. We use the standard LU factorization [109,110]:

$$K_{iajb}\Delta w^j_b + R_{ia} = 0. \tag{31}$$

Here

$$K_{iajb} = \sum_e \frac{1}{2}J_e A^{\alpha\beta}_{ij}(\mathbf{F}_e)\frac{\partial\mathcal{N}_a}{\partial x^\alpha}\frac{\partial\mathcal{N}_b}{\partial x^\beta} \tag{32}$$

is the global stiffness matrix and

$$R_{ia} = \sum_e \frac{1}{2}J_e P^\alpha_i(\mathbf{F}_e)\frac{\partial\mathcal{N}_a}{\partial x^\alpha}, \tag{33}$$

is the residual force vector; the sums run over all elements e, $\mathbf{F}_e$ is the (constant) deformation gradient, $\frac{1}{2}J_e$ is the element area, and the shape function gradients are evaluated in element e. We reiterate that summation is implied over repeated indices.

In (32) we introduced the tensor of tangential elastic moduli

$$A^{\alpha\beta}_{ij} = \frac{\partial^2\varphi_{\mathscr{D}}(\tilde{\mathbf{C}})}{\partial F^i_\alpha \partial F^j_\beta}. \tag{34}$$

Note that it can be used to find an approximate stability threshold for the homogeneous state. Indeed, if we define the acoustic tensor using the Eulerian analog of (34)

$$Q_{ij} = F^l_\alpha F^m_\beta A^{\alpha\beta}_{ij} n_l n_m, \tag{35}$$

where $\mathbf{n}$ is a unit vector, we can write the Legendre-Hadamard conditions of elastic instability in the corresponding continuum problem in the form [111–115]

$$\det(\boldsymbol{Q}) = 0. \tag{36}$$

In view of the smallness of the parameter δ in (19), the stability boundary in the discrete problem is expected to be close to the solution of (36) ensuring the existence of a first nontrivial $\mathbf{n}$. For the chosen elastic energy landscape the corresponding 'yield surface' is shown in Fig. 2.

In our numerical experiments we loaded the system quasistatically by applying the affine displacement field

$$\mathbf{u}(\alpha, \mathbf{x}) = (\bar{\mathbf{F}}(\alpha) - \mathbb{1})\mathbf{x}, \tag{37}$$

with

$$\bar{\mathbf{F}}(\alpha) = \mathbf{I} + \alpha \mathbf{e}_1 \otimes \mathbf{e}_2, \tag{38}$$

where $\mathbf{e}_A$, $A = 1, 2$, is the orthonormal basis of the reference square lattice. In this way we imposed simple shear along one of the principal slip directions with shear amplitude α serving as the loading parameter.

To simulate an effectively infinite crystal under controlled macroscopic affine deformation, we used the method of domain replication.

Specifically, starting from the basic computational domain Ω_0 with dimensions $L_x \times L_y$, we generated its minimal periodic extensions using the translation vectors

$$\mathbf{t}_{(n)} = \begin{pmatrix} n_x L_x \\ n_y L_y \end{pmatrix}, \tag{39}$$

where $\mathbf{n} = (n_x, n_y) \in \{-1, 0, 1\}^2$. Under the affine deformation (38), the position of the replicated domains relative to the central domain Ω_0 can be represented by deformed translation vectors

$$\mathbf{R}_{(n)} = \bar{\mathbf{F}}(\alpha)\mathbf{t}_{(n)}, \tag{40}$$

Now, for a node located at $\mathbf{x}_a$ in the basic domain Ω_0, its image characterized by the translation vector $\mathbf{t}_{(n)}$ is placed at

$$\mathbf{x}_{a,(n)} = \mathbf{x}_a + \mathbf{R}_{(n)}. \tag{41}$$

In this way we are guaranteed that the macroscopic deformation gradient $\bar{\mathbf{F}}(\alpha)$ is consistently applied across the periodic images of Ω_0.

After fixing through (41) the positions of all nodes for the nine domains (basic domain Ω_0 and its eight periodic images), we performed a Delaunay triangulation for the set of particles:

$$\mathcal{P} = \{\mathbf{x}_a : a \in \mathcal{I}_0\} \cup \{\mathbf{x}_{a,(n)} : a \in \mathcal{I}_0, n \neq \mathbf{0}\}, \tag{42}$$

where $\mathcal{I}_0$ denotes the set of particle indices in the basic domain. Using the obtained global triangulation $\mathcal{T}$, we selected the triangles that have at least one vertex belonging to the basic domain Ω_0. Since triangles near the boundary of the basic domain may be counted multiple times through different domain images, we need to ensure the uniqueness of the corresponding mapping. Our selection is illustrated in Fig. 3, where we show the basic domain Ω_0 (limited by the box delineated by a solid line) together with boundary triangles associated with the chosen basic domain. The proposed construction ensures that: (i) Each triangle in the computational mesh is counted exactly once, eliminating redundancy from the periodic extension; (ii) All triangles connected to the original domain are included, maintaining proper connectivity across periodic boundaries; (iii) The triangulation naturally incorporates the macroscopic deformation through the deformed positions of its periodic images.

IV. EMPIRICAL OBSERVATIONS

In our numerical experiments an ideal square crystal was represented by $N \times N$ nodes, with $N = 100, 200, 400$. The nodes were grouped into triangular finite elements. As it has been already mentioned, we impose simple shear (38) along one of the principal slip directions with shear amplitude α serving as the loading parameter. The loading was advanced in strain increments of order 10^{-6} and after each increment the displacement field was updated by the energy minimization algorithm.

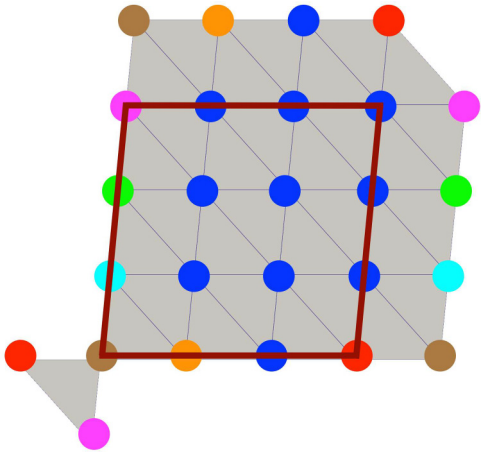


FIG. 3. The periodicity unit of the computational mesh. The basic computational domain Ω_0 is limited by the solid box. Only triangles with at least one vertex in Ω_0 are selected for the mesh (shown by the thin lines), ensuring proper connectivity across periodic boundaries while avoiding redundant counting of triangles.

Sample preparation. A pristine crystal could not be used in our experiments because real crystals, appearing in physical experiments, necessarily contain multiple dislocations. To obtain a 'generic' sample, we first 'primed' our pristine (defect-free) crystal by loading it till the point of elastic instability where the initially maintained affine configuration broke down. The associated instability marks the end of the purely elastic deformation range.

Our numerical experiments showed that such instability takes place at the value of the loading parameter α which is very close to the critical value $\alpha_c \approx 0.138$ predicted the loss of positive definiteness of the acoustic tensor (35), see [113–115]. To eliminate the degeneracy and trigger a generic path for the development of the instability we added (close to the threshold value of α) a small Gaussian quenched disorder which was removed after the system restabilized again.

The breakdown of a pristine elastic configuration took the form of a massive nucleation of dislocations resulting in a highly inhomogeneous configuration of the type shown in Fig. 4. The unfolding of the elastic instability took place in the fast computer time with the corresponding overdamped dynamics mimicked by our energy minimization algorithm. It is natural to assume that such a 'dynamics' was arrested at a state which is only marginally stable. Therefore while the configuration shown in Fig. 4 is highly defective, it is far from being random. With some abuse of language one can say that it is similar to a slowly quenched glass than to a perfect crystal.

Stress-strain relation. To study the mechanical response of the obtained 'generic' sample we continued to load it quasistatically while recording the ensuing stress-drops and the associated energy releases. The recorded stress-strain relations, corresponding to four different realization of the

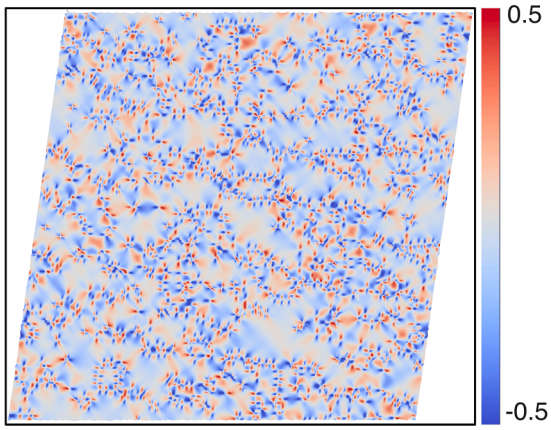


FIG. 4. Dislocated configuration emerging after a homogeneous lattice is mechanically driven to the threshold of elastic instability. Colors indicate the level of the σ_{xy} component of the Cauchy stress tensor. The highest stress levels of both signs correspond to the location of dislocation cores. Here $N = 400$.

inserted quenched disorder, are shown in Fig. 5(a). Here the solid black curve indicates the average response.

A salient feature of such a response is the presence of elastic deformations continuously interrupted by intermittent stress drops. Such drops represent plastic avalanches involving partial unlocking and restructuring of dislocation structures. The rearrangements also incorporate broadly distributed local events representing either nucleation or annihilation of dislocations.

The observed mechanical response shows a quasielastic range ending with a major (diffuse) stress drop with a subsequent formation of a stress plateau. The associated regime change can be interpreted as a transition to plastic yield. The quasielastic, preyield regime is characterized by finite overall rigidity. Instead, the postyield regime exhibits almost zero effective rigidity. In other words, while the instantaneous rigidity is finite (and similar in magnitude) in both regimes, it is in the postyield regime that it is compromised most significantly by plastic fluctuations, see Fig. 5(a).

Preyield regime. Our Fig. 5(b) illustrates the stress field in a typical preyield state A. Comparing it to Fig. 4, we observe that the overall stress level is higher but the restructuring of the dislocation pattern is relatively minor with dislocations only minimally redistributed between the preexisting locking sites. Such 'microplasticity' response is a characteristic preyield feature for both amorphous and (defective) crystalline solids [4,116–120].

As we have already seen, the quasielastic regime ends with the system-size event. It is reminiscent of a single quasibrittle plastic stress drop in well-annealed glasses and some submicron crystals [121–131]. In Figs. 5(c) and 5(d) we show the snapshots of the spatial stress configurations in the intermediate configuration B and the final configuration C. The latter can be thought of as marking a transition to postyield regime. One can see that already here the crystal starts to develop characteristic system spanning shear bands.

Grain structure development. A comparison of Figs. 5(b)–5(d) suggests that the associated global dislocational restructuring involves collective dislocation activity. Some finer aspects of the postyield configuration C are illustrated in Fig. 6 where instead of the stress field, as in our Fig. 5(d), we now show the energy distribution. The advantage of such a representation is that the locations of individual dislocations become visible.

The general observed trend is the development of low-energy patches of the original unstressed square lattice organized into a quasipolycrystalline grain texture. The elastic energy ends up being localized around dislocation-rich grain boundaries. In the inset presented in Fig. 6 we show magnification on the configuration of elastic elements. Here the individual dislocations were identified via Delaunay triangulation and the nodes with five/seven neighbors were shown in blue/red. In particular, we see the emergence of highly regular low energy $\Sigma 5$ grain boundaries. Their prevalence can be explained by the fact that the misorientation of neighboring grains is constrained by the overall compatibility of the deformation field, see [49] for a more detailed study of this issue.

Postyield regime. As we have already seen, after the termination of the diffuse quasibrittle transition stage, the ensuing postyield regime is characterized by fluctuations around an apparent yield stress. The corresponding 'dynamic attractor' can be interpreted as a nonequilibrium steady state. A representative snapshot of the microconfiguration of the crystal in a randomly chosen postyield state D is shown in Fig. 7.

First, we see significant maturation of the polycrystalline grain texture. During intermittent avalanches, characteristic of this regime, larger grains occasionally break down while smaller grains continue to emerge. One can also say that the self-organization of dislocations continues through the generation of additional length scales which contribute to the formation of a global hierarchical structure.

Second, we observe that the yield transition opens access to a much broader repertoire of relaxation mechanisms. For instance, a detailed analysis of the avalanche structure in the postyield regime (see some illustrations in the next section) reveals extended plastified regions with complex branching. Instead, in the preyield regime plastification takes place primarily in the form of isolated, linear arrangements of slipped elements.

Flow in the configurational space. Following the evolution of the system on Poincaré disk provides additional insight into the process of plastic deformation, see Figs. 8(a)–8(d). While in the reference state (pristine crystal) all configurational points are concentrated in the origin, the evolution of the loading parameter beyond the critical value α_c leads to the spreading of the configurational points with expected accumulation near the bottoms of the energy wells representing different replicas of the unstressed square lattice. In the preyield microplastic regime, see Figs. 8(a) and 8(b), the system predominantly occupies three primary energy wells immediately adjacent to the reference state. This correspond to isolated slips along the two fundamental crystalline slip planes. Instead, in the postyield regime, see Figs. 8(c) and 8(d), the formation of shear bands causes the system to populate a much broader areas of the energy landscape. While a vast majority of mesoscopic units still remains localized inside the 'locally stable' regions around the bottoms of the

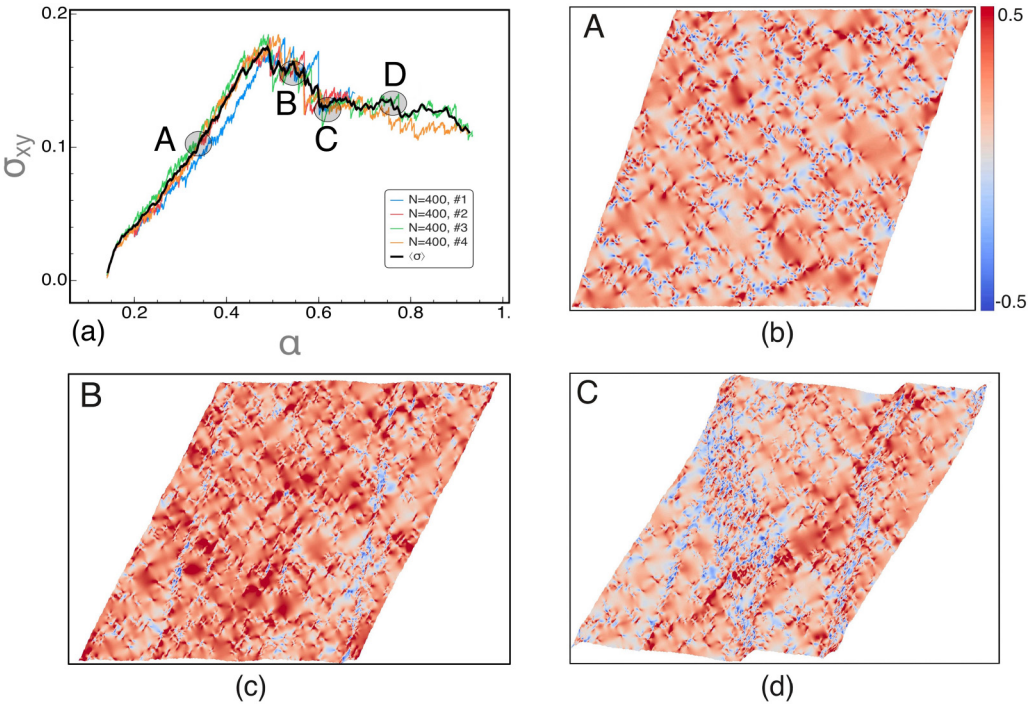


FIG. 5. (a) Stress-strain responses of four different 'generic' pseudoamorphous crystals of the type shown in Fig. 4; solid black curve indicates the average response. The stress-strain curves do not start from the origin because the global instability does not relax stresses to zero due to the emergence of self-equilibrated (residual) dislocation configuration. (b) Dislocated configuration in a typical preyield state characterizing the stage of 'microplasticity'. (c), (d) Dislocated configuration characterizing different stages of unfolding of the quasibrittle system size event. Colors indicate the level of the σ_{xy} component of the Cauchy stress tensor. In (a)–(d) N = 400.

wells, the high energy configurations corresponding to dislocation cores, are represented by the points diffusely spread over the 'locally unstable' saddle-type regions of the energy landscape.

V. POWER-LAW SCALING

An important window into the micromechanics of solids undergoing plastic flow is provided by the study of the statistical structure of plastic fluctuations [1,4,22,132–135]. In our case the relevant observables would be the energy dissipated at a single avalanche ΔW and the corresponding macroscopic stress drop $\Delta\Sigma = A\Delta\sigma_{xy}$, where A is the surface area of the sample. It is known that in amorphous solids the probability distribution of these observables is usually described by the finite-size scaling ansatz

$$P(s;L) = s^{-x}\mathcal{F}\Big(\frac{s}{L^{D_x}}\Big), \tag{43}$$

where L is the linear system size, x is the power-law exponent with $x = \tau$ for stress drops and $x = \epsilon$ for dissipated energy and D_x is the corresponding fractal dimension (D_ϵ and D_τ, respectively, for stress and energy). The scaling function $\mathcal{F}(u)$ is expected to be universal in the critical regime. In the case

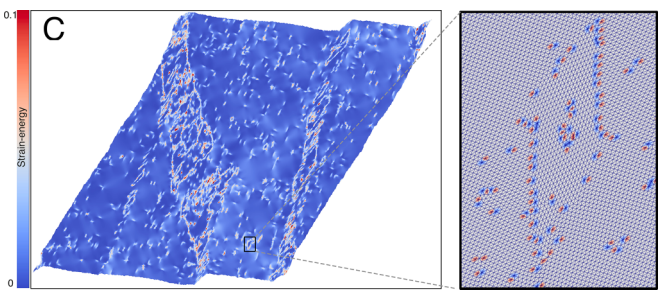


FIG. 6. The microconfiguration corresponding to the state C marked in Fig. 5. Colors indicate the magnitude of strain-energy density. The inset shows a single grain and details the dislocation structure of the grain boundaries. Here N = 400.

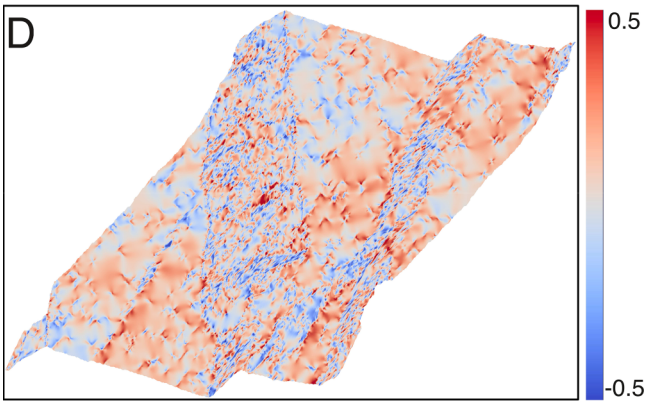


FIG. 7. Shear band development in the regime of stationary postyield plastic flow represented by the state D in Fig. 5. Here N = 400. Colors indicate the level of the shear component of the Cauchy stress tensor σ_{xy}.

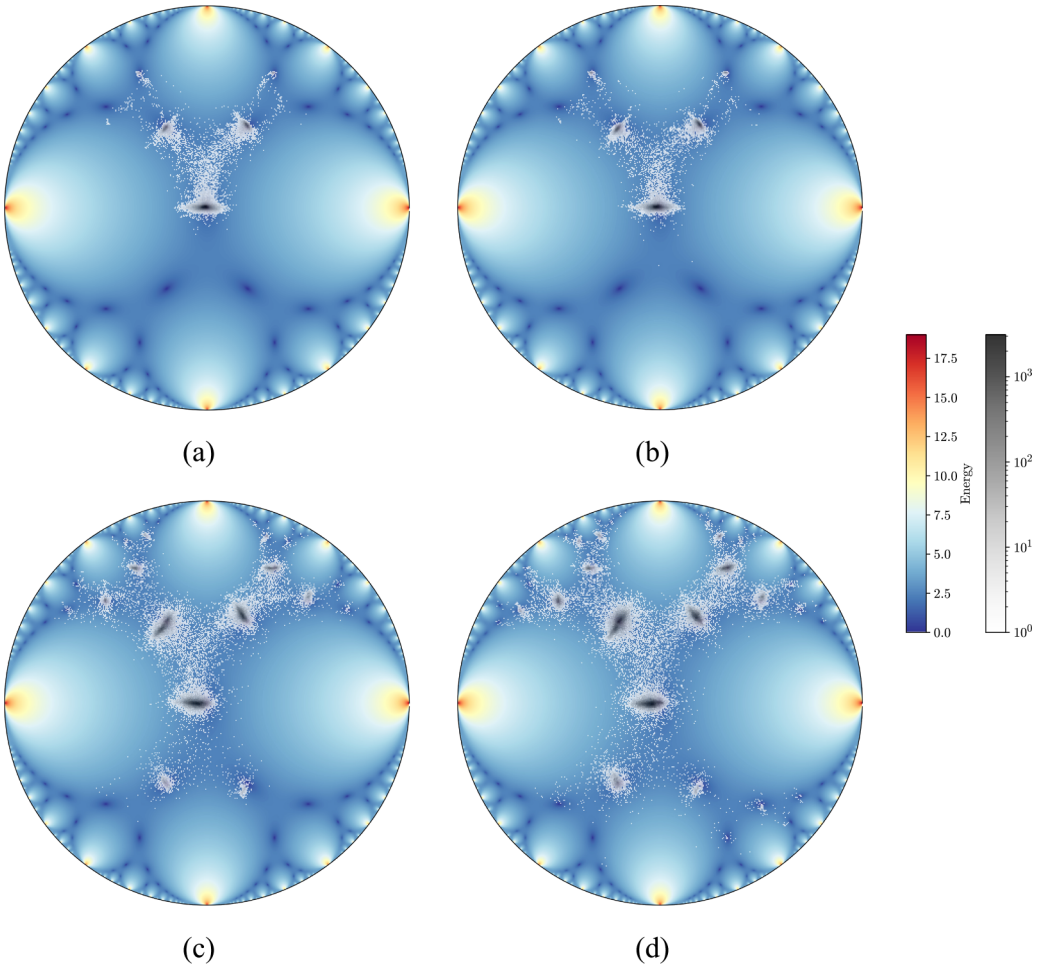


FIG. 8. Distribution of local values of the metric tensors in the configurational space projected on the Poincaré disk. Background color represents the energy landscape whose 3D representation was shown in Fig. 1(b). The color of the gray dots represents the number of the finite elements sharing the same metric tensor. (a)–(d) correspond to four values of the loading parameter α. (a) $\alpha = 0.3$ (generic preyield state), (b) $\alpha = 0.5$ (preyield state close to the yield threshold), (c) $\alpha = 0.6$ (immediate postyield state), and (d) $\alpha = 0.75$ (mature postyield state). (a) and (b) show the development of the microplastic regime and illustrate how small are the associated changes in the configuration of the elements. (c) and (d) illustrate the proliferation of plastic strain in the postyield regime with the number of populated energy wells gradually increasing.

of quasibrittle amorphous plasticity the exponents ϵ and τ were empirically found to be similar for preyield and postyield regimes while the exponents D_ϵ and D_τ were supposedly different [36,136–138].

Finite size scaling. To check the relevance of the scaling ansatz (43) in our case we introduced the rescaled variables:

$$\tilde{x}(s, L) = \frac{s}{L^{D_x}}, \tag{44}$$

and

$$\tilde{y}(s, L) = P(s; L) \cdot L^{D_{sx}x}. \tag{45}$$

The optimal parameters (x^*, D_x^*) were determined by minimizing the residual spread among the rescaled curves across the overlapping range.

First, for a discrete set of system sizes $\{L_k\}$, we computed the corresponding logarithmic data points

$$(u_{k,i}, v_{k,i}) = (\log_{10} \tilde{x}_{k,i}, \log_{10} \tilde{y}_{k,i}). \tag{46}$$

Then we determined the common logarithmic interval by identifying the overlapping limits

$$u_{\min} = \max_k \left[\min_i (u_{k,i}) \right] \tag{47}$$

and

$$u_{\max} = \min_k \left[\max_i (u_{k,i}) \right]. \tag{48}$$

For our datasets, a robust overlap domain existed near the optimal scaling exponents.

Specifically, we used a uniform grid of 80 points $\{c_j\}$ spanning the interval $[u_{\min}, u_{\max}]$. We then constructed a continuous function $\hat{v}_k(u)$ for each system size using linear interpolation between the discrete points $(u_{k,i}, v_{k,i})$. The valid set of indices $\mathcal{V}$ was defined as the subset of grid indices j ensuring that the grid points c_j lie strictly within the measured domain of all N_L interpolated curves. The quality of the collapse can be quantified by the average variance across the

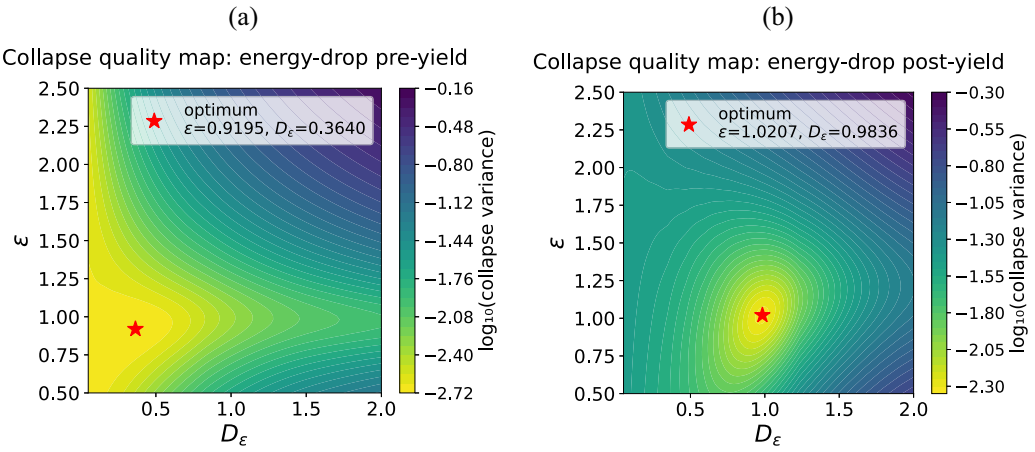


FIG. 9. Landscapes of the quality metric $\mathcal{Q}$ for the pre- and postyield regimes. (a) configuration of $\mathcal{Q}(\epsilon, D_\epsilon)$ in preyield regime, and (b) similar graph for the postyield regime. The deep, well-defined global minima in these variance surfaces allow us to choose the optimal scaling exponents and determine the associated geometric 1-σ uncertainties.

set:

$$\mathcal{Q}(x, D_x) = \frac{1}{|\mathcal{V}|}\sum_{j\in\mathcal{V}}\left(\frac{1}{N_L-1}\sum_{k=1}^{N_L}[\hat{v}_k(c_j)-\bar{v}(c_j)]^2\right), \quad (49)$$

where

$$\bar{v}(c_j) = \frac{1}{N_L}\sum_{k=1}^{N_L}\hat{v}_k(c_j) \quad (50)$$

is the mean value of the interpolated curves at the fixed grid point c_j. We employed a two-stage grid-search (first coarse, then fine) in the (x, D_x) parameter space to locate the global minimum of the variance, $\mathcal{Q}_{\min}$. The coordinates of this minimum were interpreted as providing the values of the optimal scaling exponents, (x^*, D_x^*).

To estimate the acquired uncertainty, we analyzed the curvature of the $\mathcal{Q}$ landscape immediately surrounding the minimum. For each parameter, we projected the variance onto a 1-D profile and fit it with a parabola. Because traditional statistical error models do not strictly apply to our data-collapse metric, we established an operational threshold for the error: The 1-σ confidence interval was defined as the parameter deviation required to double the variance from its optimal value (i.e., the half-width of the interval where the fit reaches $2\mathcal{Q}_{\min}$).

Main results. The computed variance landscapes and the resulting optimal data collapses are illustrated in Fig. 9 and Fig. 10. As can be seen directly from Fig. 9, a sharp, narrow minimum in the variance landscape clearly demonstrates that the scaling parameters are tightly constrained by the overlapping data. The computed scaled probability distributions for different system sizes L, illustrated in Fig. 10, fall remarkably well onto single universal master curves in both the preyield and postyield regimes. This excellent overlap, spanning several decades in both probability and avalanche sizes, serves as strong justification of the finite-size scaling ansatz (43). It suggests that for our 'generic' crystals the statistics of avalanches follows the same pattern as in their amorphous counterpart [4,21,51,64,135,139].

Marginal stability. The obtained power-law range for energy drops extends over up to six decades with preyield and postyield energy distributions sharing almost the same value of the exponent. The invariance of this exponent across the yielding transition suggests that while the spatial organization of plastic events changes drastically from local and noncooperative to global and collective, the statistical distribution of energy drops remains insensitive to these details responding only to the global organization of the underlying energy landscape [13,36,136–138,140].

The peculiar value $\epsilon = 1.0$, of the optimal exponent exhibited by the statistics of energy drops ΔW, is of considerable significance. Note first that the emergence of a power-law exponent $\epsilon \approx 1.0$ in such a distribution is a signature of an archetypically 'wild' crystal plasticity in the sense of [132]. The same value was recorded in discrete dislocation dynamics studies of disorder-free 2D samples containing a fixed number of preexisting dislocations [64,141]. It was also obtained in numerical experiments on pristine crystals conducted within a scalar version of the MTM [50].

Note next that the exponent $\epsilon \approx 1.0$ has been previously interpreted in crystal plasticity framework as representing either dislocation jamming or self-induced glassiness [21,142,143]. One reason is that exactly the same value has emerged in the studies of plastic flows in structural glasses [13,144,145]. Another reason is that the power-law exponent $\epsilon \approx 1.0$ can be linked to the hierarchical (ultrametric) organization of energy wells in the phase space [25,146–148]. More specifically, it was formally proved that in the mean-field limit of such systems the distribution of energy avalanches, characterizing their response to quasistatic deformation, is necessarily of a power law type with exponent $\epsilon \approx 1.0$.

Furthermore, in the spin glass context, where the relation between the emergence of the power-law exponent $\epsilon \approx 1.0$ and the structure of the underlying energy landscapes was reasonably well understood, it was shown that the reason behind this particular value of the exponent is the marginal stability of the system [146,149,150]. It is then not surprising that if such systems are mechanically driven, the proximity

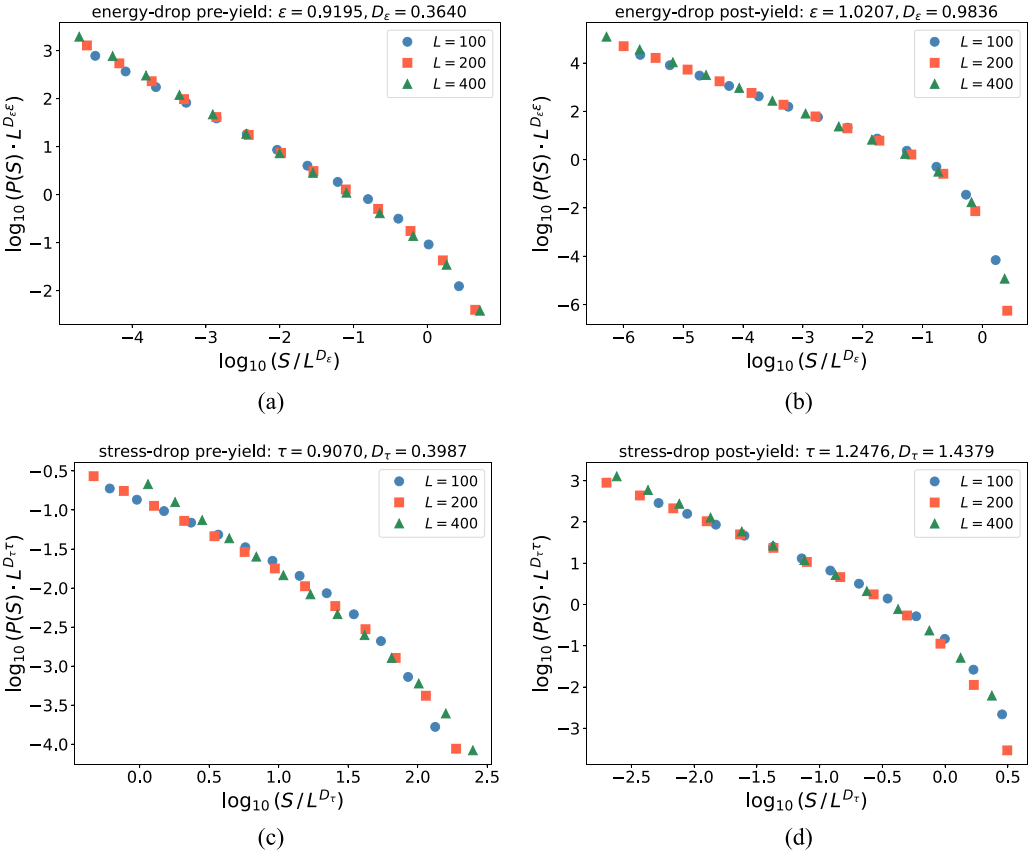


FIG. 10. Optimal data collapses of the probability distributions onto universal master curves. (a) and (b) Collapse of the energy drops ΔW in the preyield generating exponents $\epsilon = 0.9195$ and $D_\epsilon = 0.3640$ (a) and postyield regimes generating exponents $\epsilon = 1.0207$ and $D_\epsilon = 0.9836$ (b). Collapse of the macroscopic stress drops $\Delta\Sigma$ in the preyield generating exponents $\tau = 0.9070$ and $D_\tau = 0.3987$ (c) and postyield regimes, generating exponents $\tau = 1.2476$ and $D_\tau = 1.4379$ (d).

to unstable modes leads to the mixing of statics (stability) and dynamics (instability), making the mechanical response inherently intermittent [151,152]. Note also that since glasses can be viewed as liquids at a quenching threshold, their marginal stability is similar to marginality exhibited by granular matter at a jamming point.

In this perspective one can argue that, since our 'generic' crystal emerged from arrested dynamics, the associated self-generated disorder is similar to the one emerging in quenched fluids that are only marginally stable. In our case, the destabilization of the elastic phase is analogous to fluidization with subsequent restabilization bringing the system to an effectively glassy state. Interestingly, our results suggest that the implied self-induced marginality is not affected by the yield transition, which apparently does not compromise the global organization of the energy landscape while, of course, affecting the reachability of its different subdomains [153–155].

Statistics of stress drops. Consider next the obtained optimal value of the power-law exponent τ characterizing the statistics of stress drops $\Delta\Sigma$. Note first that in the preyield regime, the power-law exponents for stress and energy are rather similar, $\tau \approx \epsilon$, which suggests that the dissipated energies and the stress drops are roughly proportional, $\Delta W \sim \Delta\Sigma$. Such linear scaling implies some kind of caging. Behind it is a highly constrained dislocation motion with individual avalanches arrested by a regular arrays of obstacles. The dominant role of the obstacles in this regime may be also the reason behind the associated strong hardening.

Instead, in the postyield regime the recovered exponents τ and ϵ are markedly different. Here individual avalanches are no longer hindered by local structural constraints and one can assume that the stress drop is only constrained by the corresponding strain increment through the constitutive relations of (nonlinear) elasticity. Then, if we assume that $\Delta W \sim \Delta\Sigma^\gamma$ we can expect that $\epsilon - 1 = (\tau - 1)/\gamma$. In particular, if elasticity is linear, $\gamma = 2$, and the measured value is $\tau \approx 1.2$, we can expect that $\epsilon \approx 1.10$ which is in reasonable agreement with our measured value $\epsilon \approx 1.02$ given that the uncertainty in our relatively small system is of the order $\sim \pm 0.2$.

Fractal dimension. The computed optimal values of the exponents D_ϵ and D_τ provide information about the morphology of the plastically deforming regions. In the preyield regime we obtained the values $D_\epsilon = 0.364$ and $D_\tau = 0.3987$ and in the postyield regime the values $D_\epsilon = 0.9836$ and $D_\tau = 1.4379$. Note first that in both cases the preyield values of the corresponding cutoff parameters L^{D_x} are much smaller than their postyield values which indicates that in the postyield regime larger avalanches become more probable [18,156]. The emergent collective behavior, reflected in such broader extent of avalanche activity, reaches in postyield regime the size of the system suggesting the divergence of the characteristic length. Note next that in the preyield regime the energy

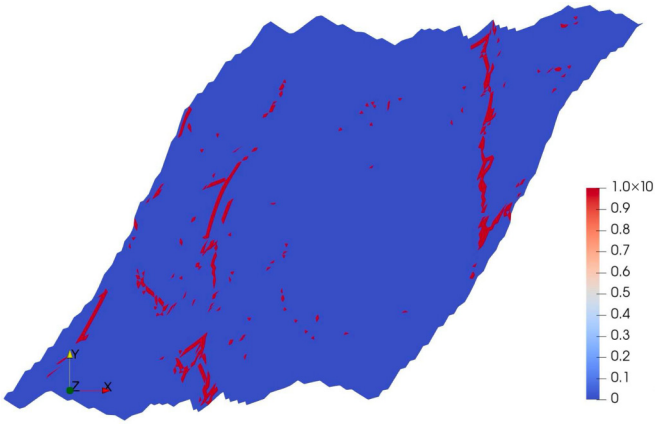


FIG. 11. Visualization of the geometric morphology of plastically active regions during typical avalanche events in the postyield regime. Domains undergoing almost 100% plastic deformation are seen as red. Plastic deformation is seen to be localized into highly correlated, system-spanning branched 1D structures, with the typical spread comparable to the linear size of the system. See also the Supplemental Material at [162] for a movie showing the spatiotemporal dynamics and morphology of plastic avalanches.

avalanches are characterized by a low fractal dimension, say $D_\epsilon \approx 0.36$, pointing towards highly localized, spatially scattered, macroscopically isolated rearrangements. Instead, in the postyield regime we obtain the value $D_\epsilon \approx 0.98$ which suggests the emergence of 1D-like system spanning bands. This reflects the highly cooperative nature of the underlying plastic deformation. The physical nature of the implied scale free cooperativity (criticality) is presently actively debated [50,157–161].

The computed values of the fractal dimensions of D_ϵ and D_τ in pre- and postyield regimes are in agreement with the different spatial structures of the corresponding avalanches. Thus, in the preyield microplasticity regime we see individual avalanches represented by highly localized, spatially scattered, microscopically isolated rearrangements. Instead, in the postyield regime such seemingly nonconnected plastification zones are replaced by highly correlated, system-spanning macroscopic structures, with plastification zones showing noticeable branching, see Fig. 11. The typical avalanches in this regime involve broadening of the shear bands and may include correlated restructuring of the grain boundaries whose total length is comparable with linear size of the system. We therefore observe a transition in structural topology from almost 0D avalanches (isolated clusters) to almost 1D avalanches (extended anisotropic bands). This qualitative picture is in full agreement with the computed values of the fractal dimension.

Elastoplastic models. The observed similarity between the structure of intermittent plastic fluctuations in amorphous and crystalline solids is not accidental. First of all, the elastoplastic models, typically used to model amorphous plasticity [26,145,163,164], are very similar to the MTM which operates within basically the same finite element setting. A superficial difference is that the fixed linear elastic propagators of the elastoplastic models are replaced in MTM by the solution 'on the fly' of the corresponding elastic problem. More important is that the phenomenological yield thresholds of elastoplastic models are replaced in the MTM by elastic instabilities originating from the nonconvexity of the energy landscape. Furthermore, if in elastoplastic models the disorder is quenched, in the MTM it is self-imposed which may or may not be of crucial importance. A salient feature of MTM is its geometrical nature originating from the exact description of finite elastic deformations. Despite these differences, the observed general agreement in the values of the computed exponents suggests that we are probably dealing in both cases with the same universality class.

VI. CONCLUSIONS

The crucial advantage of the chosen mesoscopic model is its ability to capture the specificity of crystals with different lattice symmetry at relatively low computational cost. This allowed us to demonstrate that pristine crystals can exhibit quasibrittle phenomenology which is remarkably similar to the mechanical response of well-annealed glassy materials. The similarity of the mechanical response emerges after such crystals undergo massive dislocation nucleation following the breakdown of an affine elastic configuration.

The implied nonlinear elastic instability effectively transforms a crystalline configuration into a mechanically pseudoamorphous configuration. It is still a crystal but with such a significant dislocation population that its mechanical response becomes statistically similar to the one of an amorphous solid. We argue that during such instability, dislocations self-organize into highly correlated patterns ensuring the overall mechanical marginality of the system.

In amorphous solids, the mechanical response is dominated by nonaffine relaxations that occur due to the lack of local inversion symmetry. In our 'generic' crystal emerging after the elastic instability the high density of dislocations producing local lattice misorientations effectively breaks the same type of local symmetry but at the mesoscale. As we show, this leads to a nonaffine mechanical response that is practically indistinguishable from that of a glass, even though the underlying mechanical system remains crystalline.

The marginality of the emerging mechanically pseudoamorphous solid suggests that the underlying global energy landscape is of hierarchical spin-glass nature. In other words while a full disconnectivity graph analysis is beyond our current computational abilities, one can say that we obtained an indirect evidence that our energy landscape shares key features with glassy landscapes. By referring to well-annealed glasses we conjecture that fast quenching of liquids is similar to the return to a stable state after a system size elastic instability experienced by sheared pristine crystals.

While, due to the specific nature of our 'preparation' protocol, not just any dislocated crystal is mechanically quasi-amorphous in the above sense, our results challenge the prevailing opinion that crystal and amorphous plasticity are fundamentally different phenomena. Such conclusion is usually made based on the observation that dislocations, the main carriers of plastic deformations crystals, are absent in amorphous solids. However, as our mesoscopic approach reveals, the underlying elementary mechanical events in crystal and amorphous plasticity are in fact rather similar. In particular, in both cases the elastic incompatibility evolves through inter-

mittent avalanches while the mechanical marginality reveals itself through the special values of the power-law exponents.

We simulated sufficiently large systems for the power-law exponents to be reliably extracted. The recorded 'inertial' range extends beyond five decades despite the fact that the study is conducted in the fully nonlinear tensorial setting accounting for large strains, finite rotations, and providing geometrically exact description of lattice invariant shears. It is noteworthy that the model operates with the complete set of slip directions while allowing dislocations to self-consistently nucleate and annihilate as well as to form various entanglements and locks.

The observed critical behavior and the computed value of the exponents suggest a new conceptual bridge between crystal and amorphous plasticity emphasizing the universality of the underlying criticality mechanisms In both types of systems plastic flow involves generation and propagation of elastic incompatibility, long-range interactions, and relies on threshold-type nonlinearity. Our results provide a physical explanation why in engineering plasticity essentially the same type of models are used for the description of crystal and amorphous plasticity. While the question about the universality class for crystal plasticity *vis-à-vis* that of amorphous plasticity has not been answered definitively in this paper, we showed the similarity of both, the stress-strain curves and the avalanche statistics. It is reassuring that the established similarity concerns not only the values of the power-law exponents but also the fact that both pre- and postyield avalanches are distributed in a similar way.

Regarding crystal plasticity proper, the revealed convergence of the values of critical exponents obtained using different computational approaches, suggests that at least in 2D, the associated scaling behavior can be already captured by the most basic approaches such as DDD. A claim of this type, however, could not had been made before it was confirmed in the framework of MTM, which is geometrically exact and fully tensorial theory relying only minimally on phenomenology.

While the proposed mesoscopic framework to crystal plasticity is very revealing, many important issues remain to be addressed. Thus, it is important to systematically compare the obtained core structures of individual dislocations with the results of molecular dynamics. Also recall, that the submesoscale (subgrid) phenomena are described in the current version of the model only at the coarse grained level. For instance, while our mesoscale dislocations interact like the actual physical dislocations, their number is naturally smaller than in the actual crystal. The corresponding rescaling can be made based on the detailed study of the dislocational structure of grain boundaries. Adaptation of the model to realistic 3D crystals will allow one to distinguish between edge and screw dislocations opening the way to the adequate account of such physically important effects as dislocation climb, cross slip, and forest hardening. To be physically realistic, the comprehensive version of the model should incorporate finite temperature effects and account in this way for thermally activated dislocation reactions [165,166].

ACKNOWLEDGMENTS

The authors thank N. Gorbushin for helpful comments. The work of O.U.S. was supported by the Grants No. ANR-21-CE08-MESOCRYSP, No. ANR-20-CE91-0010, and No. ANR-24-CE91-0002. L.T. was supported by the Grants No. ANR-21-CE08-MESOCRYSP and No. ERC-H2020-MSCA-RISE-2020-101008140.

DATA AVAILABILITY

There are no publicly available research data or software supporting this manuscript. Requests for further information or data should be sent to the authors.

[1] M. Zaiser, Scale invariance in plastic flow of crystalline solids, Adv. Phys. **55**, 185 (2006).

[2] W. Jian, M. Xiao, W. Sun, and W. Cai, Prediction of yield surface of single crystal copper from discrete dislocation dynamics and geometric learning, J. Mech. Phys. Solids **186**, 105577 (2024).

[3] M. Ortiz, Plastic yielding as a phase transition, J. Appl. Mech. **66**, 289 (1999).

[4] S. Papanikolaou, Y. Cui, and N. Ghoniem, Avalanches and plastic flow in crystal plasticity: An overview, Modell. Simul. Mater. Sci. Eng. **26**, 013001 (2018).

[5] J. Kosterlitz, Kosterlitz–Thouless physics: A review of key issues, Rep. Prog. Phys. **79**, 026001 (2016).

[6] M. Khantha and V. Vitek, Mechanism of yielding in dislocation-free crystals at finite temperatures—Part I. Theory, Acta Mater. **45**, 4675 (1997).

[7] T. Hochrainer, S. Sandfeld, M. Zaiser, and P. Gumbsch, Continuum dislocation dynamics: Towards a physical theory of crystal plasticity, J. Mech. Phys. Solids **63**, 167 (2014).

[8] J. S. Langer, Statistical thermodynamics of crystal plasticity, J. Stat. Phys. **175**, 531 (2019).

[9] P. M. Derlet and R. Maaß, The stress statistics of the first pop-in or discrete plastic event in crystal plasticity, J. Appl. Phys. **120**, 225101 (2016).

[10] P. D. Ispánovity, I. Groma, G. Györgyi, F. F. Csikor, and D. Weygand, Submicron plasticity: Yield stress, dislocation avalanches, and velocity distribution, Phys. Rev. Lett. **105**, 085503 (2010).

[11] K. M. Kamani and S. A. Rogers, Brittle and ductile yielding in soft materials, Proc. Natl. Acad. Sci. USA **121**, e2401409121 (2024).

[12] L. Berthier, G. Biroli, M. L. Manning, and F. Zamponi, Yielding and plasticity in amorphous solids, Nat. Rev. Phys. **7**, 313 (2024).

[13] B. Shang, P. Guan, and J. L. Barrat, Elastic avalanches reveal marginal behavior in amorphous solids, Proc. Natl. Acad. Sci. USA **117**, 86 (2020).

[14] J. Shang, Y. Wang, D. Pan, Y. Jin, and J. Zhang, The yielding of granular matter is marginally stable and critical, Proc. Natl. Acad. Sci. USA **121**, e2402843121 (2024).

[15] M. Singh, M. Ozawa, and L. Berthier, Brittle yielding of amorphous solids at finite shear rates, Phys. Rev. Mater. **4**, 025603 (2020).

[16] D. Richard, E. Lerner, and E. Bouchbinder, Brittle-to-ductile transitions in glasses: Roles of soft defects and loading geometry, MRS Bull. **46**, 902 (2021).

[17] J. Pollard and S. M. Fielding, Yielding, shear banding, and brittle failure of amorphous materials, Phys. Rev. Res. **4**, 043037 (2022).

[18] J. Lin, E. Lerner, A. Rosso, and M. Wyart, Scaling description of the yielding transition in soft amorphous solids at zero temperature, Proc. Natl. Acad. Sci. USA **111**, 14382 (2014).

[19] G. Parisi, I. Procaccia, C. Rainone, and M. Singh, Shear bands as manifestation of a criticality in yielding amorphous solids, Proc. Natl. Acad. Sci. USA **114**, 5577 (2017).

[20] P. M. Derlet and R. Maaß, Micro-plasticity in a fragile model binary glass, Acta Mater. **209**, 116771 (2021).

[21] A. Lehtinen, G. Costantini, M. J. Alava, S. Zapperi, and L. Laurson, Glassy features of crystal plasticity, Phys. Rev. B **94**, 064101 (2016).

[22] J. P. Sethna, M. K. Bierbaum, K. A. Dahmen, C. P. Goodrich, J. R. Greer, L. X. Hayden, J. P. Kent-Dobias, E. D. Lee, D. B. Liarte, X. Ni, K. N. Quinn, A. Raju, D. Zeb Rocklin, A. Shekhawat, and S. Zapperi, Deformation of crystals: Connections with statistical physics, Annu. Rev. Mater. Res. **47**, 217 (2017).

[23] M. Ovaska, A. Lehtinen, M. J. Alava, L. Laurson, and S. Zapperi, Excitation spectra in crystal plasticity, Phys. Rev. Lett. **119**, 265501 (2017).

[24] A. Zaccone and E. Scossa-Romano, Approximate analytical description of the nonaffine response of amorphous solids, Phys. Rev. B **83**, 184205 (2011).

[25] M. Müller and M. Wyart, Marginal stability in structural, spin, and electron glasses, Annu. Rev. Condens. Matter Phys. **6**, 177 (2015).

[26] A. Nicolas, E. E. Ferrero, K. Martens, and J. L. Barrat, Deformation and flow of amorphous solids: Insights from elastoplastic models, Rev. Mod. Phys. **90**, 045006 (2018).

[27] D. Rodney, A. Tanguy, and D. Vandembroucq, Modeling the mechanics of amorphous solids at different length scale and time scale, Modell. Simul. Mater. Sci. Eng. **19**, 083001 (2011).

[28] M. Popović, T. W. J. de Geus, and M. Wyart, Elastoplastic description of sudden failure in athermal amorphous materials during quasistatic loading, Phys. Rev. E **98**, 040901(R) (2018).

[29] A. Tanguy, Elasto-plastic behavior of amorphous materials: A brief review, C. R. Phys. **22**, 117 (2021).

[30] M. Talamali, V. Petäjä, D. Vandembroucq, and S. Roux, Strain localization and anisotropic correlations in a mesoscopic model of amorphous plasticity, C. R. Mec. **340**, 275 (2012).

[31] J. T. Parley and P. Sollich, Ductile and brittle yielding of athermal amorphous solids: A mean-field paradigm beyond the random-field Ising model, Phys. Rev. E **110**, 045002 (2024).

[32] S. Karmakar, E. Lerner, and I. Procaccia, Statistical physics of the yielding transition in amorphous solids, Phys. Rev. E **82**, 055103(R) (2010).

[33] M. Ozawa, L. Berthier, G. Biroli, A. Rosso, and G. Tarjus, Random critical point separates brittle and ductile yielding transitions in amorphous materials, Proc. Natl. Acad. Sci. USA **115**, 6656 (2018).

[34] T. Divoux, E. Agoritsas, S. Aime, C. Barentin, J.-L. Barrat, R. Benzi, L. Berthier, D. Bi, G. Biroli, D. Bonn, P. Bourrianne, M. Bouzid, E. Del Gado, H. Delanoë-Ayari, K. Farain, S. Fielding, M. Fuchs, J. van der Gucht, S. Henkes, M. Jalaal, *et al.*, Ductile-to-brittle transition and yielding in soft amorphous materials: Perspectives and open questions, Soft Matter **20**, 6868 (2024).

[35] G. Picard, A. Ajdari, F. Lequeux, and L. Bocquet, Elastic consequences of a single plastic event: A step towards the microscopic modeling of the flow of yield stress fluids, Eur. Phys. J. E, **15**, 371 (2004).

[36] Z. Budrikis, D. Castellanos, S. Sandfeld, M. Zaiser, and S. Zapperi, Universal features of amorphous plasticity, Nat. Commun. **8**, 15928 (2017).

[37] W. Cai, A. Arsenlis, C. R. Weinberger, and V. V. Bulatov, A non-singular continuum theory of dislocations, J. Mech. Phys. Solids **54**, 561 (2006).

[38] M. Moshe, I. Levin, H. Aharoni, R. Kupferman, and E. Sharon, Geometry and mechanics of two-dimensional defects in amorphous materials, Proc. Natl. Acad. Sci. USA **112**, 10873 (2015).

[39] M. Baggioli, M. Landry, and A. Zaccone, Deformations, relaxation, and broken symmetries in liquids, solids, and glasses: A unified topological field theory, Phys. Rev. E **105**, 024602 (2022).

[40] M. J. Bowick and L. Giomi, Two-dimensional matter: Order, curvature and defects, Adv. Phys. **58**, 449 (2009).

[41] M. Katanaev and I. Volovich, Theory of defects in solids and three-dimensional gravity, Ann. Phys. **216**, 1 (1992).

[42] F. Sozio and A. Yavari, Riemannian and Euclidean material structures in anelasticity, Math. Mech. Solids **25**, 1267 (2020).

[43] O. U. Salman and L. Truskinovsky, Minimal integer automaton behind crystal plasticity, Phys. Rev. Lett. **106**, 175503 (2011).

[44] O. U. Salman and L. Truskinovsky, On the critical nature of plastic flow: One and two dimensional models, Int. J. Eng. Sci. **59**, 219 (2012).

[45] R. Baggio, E. Arbib, P. Biscari, S. Conti, L. Truskinovsky, G. Zanzotto, and O. U. Salman, Landau-type theory of planar crystal plasticity, Phys. Rev. Lett. **123**, 205501 (2019).

[46] O. U. Salman, R. Baggio, B. Bacroix, G. Zanzotto, N. Gorbushin, and L. Truskinovsky, Discontinuous yielding of pristine micro-crystals, C. R. Phys. **22**, 201 (2021).

[47] N. Perchikov and L. Truskinovsky, Quantized plastic deformation, J. Mech. Phys. Solids **190**, 105704 (2024).

[48] R. Baggio, O. U. Salman, and L. Truskinovsky, Homogeneous nucleation of dislocations as a pattern formation phenomenon, Eur. J. Mech. A/Solids **99**, 104897 (2023).

[49] R. Baggio, O. U. Salman, and L. Truskinovsky, Inelastic rotations and pseudoturbulent plastic avalanches in crystals, Phys. Rev. E **107**, 025004 (2023).

[50] P. Zhang, O. U. Salman, J. Weiss, and L. Truskinovsky, Variety of scaling behaviors in nanocrystalline plasticity, Phys. Rev. E **102**, 023006 (2020).

[51] J. Weiss, P. Zhang, O. U. Salman, G. Liu, and L. Truskinovsky, Fluctuations in crystalline plasticity, C. R. Phys. **22**, 163 (2021).

[52] A. Arsenlis, W. Cai, M. Tang, M. Rhee, T. Oppelstrup, G. Hommes, T. G. Pierce, and V. V. Bulatov, Enabling strain hardening simulations with dislocation dynamics, Modell. Simul. Mater. Sci. Eng. **15**, 553 (2007).

[53] L. A. Zepeda-Ruiz, A. Stukowski, T. Oppelstrup, N. Bertin, N. R. Barton, R. Freitas, and V. V. Bulatov, Atomistic insights into metal hardening, Nat. Mater. **20**, 315 (2021).

[54] M. Ponga, K. Bhattacharya, and M. Ortiz, Large scale *ab-initio* simulations of dislocations, J. Comput. Phys. **407**, 109249 (2020).

[55] P. Lafourcade, G. Ewald, T. Carrard, and C. Denoual, Extraction of slip systems and twinning variants from a Lagrangian analysis of molecular dynamics simulations, Mech. Mater. **200**, 105189 (2025).

[56] P. Y. Chan, G. Tsekenis, J. Dantzig, K. A. Dahmen, and N. Goldenfeld, Plasticity and dislocation dynamics in a phase field crystal model, Phys. Rev. Lett. **105**, 015502 (2010).

[57] M. Salvalaglio, L. Angheluta, Z.-F. Huang, A. Voigt, K. R. Elder, and J. Viñals, A coarse-grained phase-field crystal model of plastic motion, J. Mech. Phys. Solids **137**, 103856 (2020).

[58] Z. Zhong, Y. Huang, Y. Gao, R. Li, S. Yao, K. Wang, W. Zhu, and W. Hu, Phase field crystal model simulation of transonic dislocations and mode II crack propagation, Physica B **706**, 417154 (2025).

[59] M. Javanbakht and V. I. Levitas, Phase field approach to dislocation evolution at large strains: Computational aspects, Int. J. Solids Struct. **82**, 95 (2016).

[60] I. J. Beyerlein and A. Hunter, Understanding dislocation mechanics at the mesoscale using phase field dislocation dynamics, Philos. Trans. A: Math. Phys. Eng. Sci. **374**, 20150166 (2016).

[61] M. Koslowski, A. M. Cuitiño, and M. Ortiz, A phase-field theory of dislocation dynamics, strain hardening and hysteresis in ductile single crystals, J. Mech. Phys. Solids **50**, 2597 (2002).

[62] Y. U. Wang, Y. M. Jin, and A. G. Khachaturyan, Phase field microelasticity modeling of dislocation dynamics near free surface and in heteroepitaxial thin films, Acta Mater. **51**, 4209 (2003).

[63] B. Devincre, T. Hoc, and L. Kubin, Dislocation mean free paths and strain hardening of crystals, Science **320**, 1745 (2008).

[64] P. D. Ispánovity, L. Laurson, M. Zaiser, I. Groma, S. Zapperi, and M. J. Alava, Avalanches in 2D dislocation systems: Plastic yielding is not depinning, Phys. Rev. Lett. **112**, 235501 (2014).

[65] D. Gómez-García, B. Devincre, and L. P. Kubin, Dislocation patterns and the similitude principle: 2.5D mesoscale simulations, Phys. Rev. Lett. **96**, 125503 (2006).

[66] G. Po, M. Lazar, D. Seif, and N. Ghoniem, Singularity-free dislocation dynamics with strain gradient elasticity, J. Mech. Phys. Solids **68**, 161 (2014).

[67] S. Lu, J. Zhao, M. Huang, Z. Li, G. Kang, and X. Zhang, Multiscale discrete dislocation dynamics study of gradient nano-grained materials, Int. J. Plast. **156**, 103356 (2022).

[68] N. Bertin, V. V. Bulatov, and F. Zhou, Learning dislocation dynamics mobility laws from large-scale MD simulations, npj Comput. Mater. **10**, 192 (2024).

[69] T. Nasir Tak and P. J. Guruprasad, A discrete dislocation dynamics framework for modelling plasticity in two-phase polycrystals, Modell. Simul. Mater. Sci. Eng. **33**, 045001 (2025).

[70] K. Starkey, G. Winther, and A. El-Azab, Theoretical development of continuum dislocation dynamics for finite-deformation crystal plasticity at the mesoscale, J. Mech. Phys. Solids **139**, 103926 (2020).

[71] Y. Zhang, R. Wu, and M. Zaiser, Continuum dislocation dynamics as a phase field theory with conserved order parameters: formulation and application to dislocation patterning, Modell. Simul. Mater. Sci. Eng. **33**, 035011 (2025).

[72] A. Acharya, An action for nonlinear dislocation dynamics, J. Mech. Phys. Solids **161**, 104811 (2022).

[73] A. Acharya, A. Roy, and A. Sawant, Continuum theory and methods for coarse-grained, mesoscopic plasticity, Scr. Mater. **54**, 705 (2006).

[74] D. Rodney and R. Phillips, Structure and strength of dislocation junctions: An atomic level analysis, Phys. Rev. Lett. **82**, 1704 (1999).

[75] B. Van Koten and B. Luskin, Analysis of energy-based blended quasi-continuum approximations, SIAM J. Numer. Anal. **49**, 2182 (2011).

[76] R. Miller and E. Tadmor, The quasicontinuum method: Overview, applications and current directions, J. Comput.-Aided Mater. Des. **9**, 203 (2002).

[77] Z. Zhang, J. Zhang, Y. Ni, C. Wang, K. Jiang, and X. Ren, *Multiscale Simulation of Surface Defect Influence in Nanoindentation by the Quasi-Continuum Method in Proceedings* (MDPI, 2018), Vol. 2, p. 1113.

[78] P. Engel, *Geometric Crystallography: An Axiomatic Introduction to Crystallography* (Springer, Netherlands, 1986).

[79] L. Michel, Fundamental concepts for the study of crystal symmetry, Phys. Rep. **341**, 265 (2001).

[80] R. L. E. Schwarzenberger, Classification of crystal lattices, Proc. Cambridge Philos. Soc. **72**, 325 (1972).

[81] M. Pitteri and G. Zanzotto, *Continuum Models for Phase Transitions and Twinning in Crystals* (Chapman and Hall/CRC, Boca Raton, 2002).

[82] J. L. Ericksen, Nonlinear elasticity of diatomic crystals, Int. J. Solids Struct. **6**, 951 (1970).

[83] J. L. Ericksen, in *Nonlinear Elasticity*, edited by R. W. Dickey (Academic Press, New York, 1973), pp. 161–173.

[84] J. L. Ericksen, Special topics in elastostatics, Adv. Appl. Mech. **17**, 189 (1977).

[85] J. L. Ericksen, Some phase transitions in crystals, Arch. Ration. Mech. Anal. **73**, 99 (1980).

[86] J. L. Ericksen, Weak martensitic transformations in Bravais lattices, Arch. Ration. Mech. Anal. **107**, 23 (1989).

[87] G. Parry, On the elasticity of monatomic crystals, Math. Proc. Cambridge Philos. Soc. **80**, 189 (1976).

[88] G. P. Parry, On the crystallographic point groups and on Cauchy symmetry, in *Mathematical Proceedings of the Cambridge Philosophical Society* (Cambridge University Press, 1977), pp. 165–175.

[89] G. P. Parry, Low-dimensional lattice groups for the continuum mechanics of phase transitions in crystals, Arch. Ration. Mech. Anal. **145**, 1 (1998).

[90] I. Folkins, Functions of two-dimensional Bravais lattices, J. Math. Phys. **32**, 1965 (1991).

[91] S. Conti and G. Zanzotto, A variational model for reconstructive phase transformations in crystals, and their relation to dislocations and plasticity, Arch. Ration. Mech. Anal. **173**, 69 (2004).

[92] K. Bhattacharya, S. Conti, G. Zanzotto, and J. Zimmer, Crystal symmetry and the reversibility of martensitic transformations, Nature (London) **428**, 55 (2004).

[93] M. Koslowski, R. LeSar, and R. Thomson, Avalanches and scaling in plastic deformation, Phys. Rev. Lett. **93**, 125502 (2004).

[94] C. Denoual, A. M. Caucci, L. Soulard, and Y. P. Pellegrini, Phase-field reaction-pathway kinetics of martensitic transformations in a model Fe_3Ni alloy, Phys. Rev. Lett. **105**, 035703 (2010).

[95] Y. Gao, Y. Wang, and Y. Zhang, Deformation pathway and defect generation in crystals: A combined group theory and graph theory description, IUCrJ **6**, 96 (2019).

[96] P. Biscari, M. Urbano, A. Zanzottera, and G. Zanzotto, Intermittency in crystal plasticity informed by lattice symmetry, J. Elast. **123**, 85 (2016).

[97] E. Arbib, P. Biscari, C. Patriarca, and G. Zanzotto, Ericksen-Landau modular strain energies for reconstructive phase transformations in 2D crystals, J. Elast. **155**, 747 (2024).

[98] Y. Gao, Y. Zhang, and Y. Wang, Determination of twinning path from broken symmetry: A revisit to deformation twinning in BCC metals, Acta Mater. **196**, 280 (2020).

[99] Y. Gao, A Cayley graph description of the symmetry breaking associated with deformation and structural phase transitions in metallic materials, Materialia **9**, 100588 (2020).

[100] Y. Gao, T. Yu, and Y. Wang, Phase transformation graph and transformation pathway engineering for shape memory alloys, Shap. Mem. Superelasticity **6**, 115 (2020).

[101] Y. Gao, Y. Zhang, L. K. Aagesen, J. Yu, M. Long, and Y. Wang, Defect-free plastic deformation through dimensionality reduction and self-annihilation of topological defects in crystalline solids, Phys. Rev. Res. **2**, 013146 (2020).

[102] E. Arbib, P. Biscari, L. Bortoloni, C. Patriarca, and G. Zanzotto, Crystal elasto-plasticity on the Poincaré half-plane, Int. J. Plast. **130**, 102728 (2020).

[103] E. Arbib, N. Barrera, P. Biscari, and G. Zanzotto, Reconstructive martensitic phase transitions: Intermittency, anti-transformation, plasticity, irreversibility, J. Appl. Mech. **92**, 081007 (2025).

[104] P. Engel, *Geometric Crystallography: An Axiomatic Introduction to Crystallography* (Springer Science & Business Media, Dordrecht, 2012).

[105] G. Puglisi and L. Truskinovsky, Thermodynamics of rate-independent plasticity, J. Mech. Phys. Solids **53**, 655 (2005).

[106] B. M. Irons, Engineering applications of numerical integration in stiffness methods, AIAA J. **4**, 2035 (1966).

[107] J. H. Bramble and M. Zlámal, Triangular elements in the finite element method, Math. Comput. **24**, 809 (1970).

[108] S. Bochkanov and V. Bystritsky, Available from: www.alglib.net (2013).

[109] C. Sanderson and R. Curtin, Armadillo: A template-based C++ library for linear algebra, J. Open Source Softw. **1**, 26 (2016).

[110] M. Fishman, S. White, and E. Stoudenmire, The ITensor software library for tensor network calculations, SciPost Phys. Codebases 4 (2022).

[111] R. W. Ogden, *Non-linear Elastic Deformations* (Courier Corporation, 1997).

[112] Y. Grabovsky and L. Truskinovsky, Normality condition in elasticity, J. Nonlinear Sci. **24**, 1125 (2014).

[113] H. C. Simpson and S. J. Spector, in *Mechanics and Thermodynamics of Continua: A Collection of Papers Dedicated to BD Coleman on His Sixtieth Birthday* (Springer Berlin Heidelberg, Berlin, Heidelberg, 1989), pp. 159–179.

[114] Y. Grabovsky and L. Truskinovsky, Marginal material stability, J. Nonlinear Sci. **23**, 891 (2013).

[115] D. J. Steigmann, M. Bîrsan, and M. Shirani, in *Lecture Notes on the Theory of Plates and Shells: Classical and Modern Developments* (Springer Nature Switzerland, Cham, 2023), pp. 61–76.

[116] R. Maaß and P. M. Derlet, Micro-plasticity and recent insights from intermittent and small-scale plasticity, Acta Mater. **143**, 338 (2018).

[117] G. Sparks and R. Maaß, Nontrivial scaling exponents of dislocation avalanches in microplasticity, Phys. Rev. Mater. **2**, 120601(R) (2018).

[118] G. Sparks, Y. Cui, G. Po, Q. Rizzardi, J. Marian, and R. Maaß, Avalanche statistics and the intermittent-to-smooth transition in microplasticity, Phys. Rev. Mater. **3**, 080601(R) (2019).

[119] Q. Rizzardi, P. M. Derlet, and R. Maaß, Intermittent microplasticity in the presence of a complex microstructure, Phys. Rev. Mater. **6**, 073602 (2022).

[120] J. Duan, Y. J. Wang, L. H. Dai, and M. Q. Jiang, Elastic interactions of plastic events in strained amorphous solids before yield, Phys. Rev. Mater. **7**, 013601 (2023).

[121] H. Bei, S. Shim, G. M. Pharr, and E. P. George, Effects of pre-strain on the compressive stress–strain response of Mo-alloy single-crystal micropillars, Acta Mater. **56**, 4762 (2008).

[122] D. Chrobak, N. Tymiak, A. Beaber, O. Ugurlu, W. W. Gerberich, and R. Nowak, Deconfinement leads to changes in the nanoscale plasticity of silicon, Nat. Nanotechnol. **6**, 480 (2011).

[123] Z. Wang, Z. Shan, J. Li, J. Sun, and E. Ma, Pristine-to-pristine regime of plastic deformation in submicron-sized single crystal gold particles, Acta Mater. **60**, 1368 (2012).

[124] Y. Cui, G. Po, and N. Ghoniem, Influence of loading control on strain bursts and dislocation avalanches at the nanometer and micrometer scale, Phys. Rev. B **95**, 064103 (2017).

[125] J. R. Greer and J. T. M. De Hosson, Plasticity in small-sized metallic systems: Intrinsic versus extrinsic size effect, Prog. Mater. Sci. **56**, 654 (2011).

[126] S. S. Brenner, Tensile strength of whiskers, J. Appl. Phys. **27**, 1484 (1956).

[127] S. S. Brenner, Growth and properties of "whiskers", Science **128**, 569 (1958).

[128] A. Sharma, J. Hickman, N. Gazit, E. Rabkin, and Y. Mishin, Nickel nanoparticles set a new record of strength, Nat. Commun. **9**, 4102 (2018).

[129] D. Mordehai, O. David, and R. Kositski, Nucleation-controlled plasticity of metallic nanowires and nanoparticles, Adv. Mater. **30**, 1706710 (2018).

[130] E. T. Lilleodden and W. D. Nix, Microstructural length-scale effects in the nanoindentation behavior of thin gold films, Acta Mater. **54**, 1583 (2006).

[131] S. G. Corcoran, R. J. Colton, E. T. Lilleodden, and W. W. Gerberich, Anomalous plastic deformation at surfaces:

Nanoindentation of gold single crystals, Phys. Rev. B **55**, R16057 (1997).
[132] J. Weiss, W. B. Rhouma, T. Richeton, S. Dechanel, F. Louchet, and L. Truskinovsky, From mild to wild fluctuations in crystal plasticity, Phys. Rev. Lett. **114**, 105504 (2015).
[133] J. M. Tarp, L. Angheluta, J. Mathiesen, and N. Goldenfeld, Intermittent dislocation density fluctuations in crystal plasticity from a phase-field crystal model, Phys. Rev. Lett. **113**, 265503 (2014).
[134] M. C. Miguel and S. Zapperi, Fluctuations in plasticity at the microscale, Science **312**, 1151 (2006).
[135] M. J. Alava, L. Laurson, and S. Zapperi, Crackling noise in plasticity, Eur. Phys. J. Spec. Top. **223**, 2353 (2014).
[136] B. Tyukodi, C. A. Lemarchand, J. S. Hansen, and D. Vandembroucq, Finite-size effects in a model for plasticity of amorphous composites, Phys. Rev. E **93**, 023004 (2016).
[137] E. Lerner, I. Procaccia, C. Rainone, and M. Singh, Protocol dependence of plasticity in ultrastable amorphous solids, Phys. Rev. E **98**, 063001 (2018).
[138] M. Ozawa, L. Berthier, G. Biroli, and G. Tarjus, Rare events and disorder control the brittle yielding of well-annealed amorphous solids, Phys. Rev. Res. **4**, 023227 (2022).
[139] J. P. Sethna, K. A. Dahmen, and C. R. Myers, Crackling noise, Nature (London) **410**, 242 (2001).
[140] N. Oyama, H. Mizuno, and A. Ikeda, Unified view of avalanche criticality in sheared glasses, Phys. Rev. E **104**, 015002 (2021).
[141] H. Salmenjoki, L. Laurson, and M. J. Alava, Avalanche correlations and stress-strain curves in discrete dislocation plasticity, Phys. Rev. Mater. **5**, 073601 (2021).
[142] M. Ovaska, L. Laurson, and M. J. Alava, Quenched pinning and collective dislocation dynamics, Sci. Rep. **5**, 10580 (2015).
[143] X. Zhang, X. Zhang, Q. Li, and F. Shang, Strain avalanches in microsized single crystals: Avalanche size predicted by a continuum crystal plasticity model, Chin. Phys. Lett. **33**, 106401 (2016).
[144] B. Tyukodi, D. Vandembroucq, and C. E. Maloney, Avalanches, thresholds, and diffusion in mesoscale amorphous plasticity, Phys. Rev. E **100**, 043003 (2019).
[145] E. E. Ferrero and E. A. Jagla, Criticality in elastoplastic models of amorphous solids with stress-dependent yielding rates, Soft Matter **15**, 9041 (2019).
[146] S. Franz and S. Spigler, Mean-field avalanches in jammed spheres, Phys. Rev. E **95**, 022139 (2017).
[147] L. Berthier, G. Biroli, P. Charbonneau, E. I. Corwin, S. Franz, and F. Zamponi, Gardner physics in amorphous solids and beyond, J. Chem. Phys. **151**, 010901 (2019).
[148] R. C. Dennis and E. I. Corwin, Jamming energy landscape is hierarchical and ultrametric, Phys. Rev. Lett. **124**, 078002 (2020).
[149] F. Pázmándi, G. Zaránd, and G. T. Zimányi, Self-organized criticality in the hysteresis of the Sherrington-Kirkpatrick model, Phys. Rev. Lett. **83**, 1034 (1999).
[150] P. Le Doussal, M. Müller, and K. J. Wiese, Equilibrium avalanches in spin glasses, Phys. Rev. B.Cond. Matt. Mater. Phys. **85**, 214402 (2012).
[151] K. Lamp, N. Küchler, and J. Horbach, Brittle yielding in supercooled liquids below the critical temperature of mode coupling theory, J. Chem. Phys. **157**, 034501 (2022).
[152] S. Rossi and G. Tarjus, Emergence of a random field at the yielding transition of a mean-field elasto-plastic model, J. Stat. Mech. (2022) 093301.
[153] I. Regev and T. Lookman, The irreversibility transition in amorphous solids under periodic shear, in *Avalanches in Functional Materials and Geophysics*, edited by E. Salje, A. Saxena, and A. Planes (Springer International Publishing, Cham, 2017), pp. 227–259.
[154] I. Regev and T. Lookman, Critical diffusivity in the reversibilityirreversibility transition of amorphous solids under oscillatory shear, J. Phys.: Cond. Matt. **31**, 045101 (2019).
[155] I. Regev, I. Attia, K. Dahmen, S. Sastry, and M. Mungan, Topology of the energy landscape of sheared amorphous solids and the irreversibility transition, Phys. Rev. E **103**, 062614 (2021).
[156] C. Ruscher and J. Rottler, Avalanches in the athermal quasistatic limit of sheared amorphous solids: An atomistic perspective, Tribol. Lett. **69**, 64 (2021).
[157] G. Grinstein, *Scale Invariance, Interfaces, and Non-Equilibrium Dynamics* (Springer US, Boston, MA, 1995), pp. 261–293.
[158] A. Zippelius, M. Fuchs, A. Rosso, J. P. Sethna, and M. Wyart, Emergent dynamics in glasses and disordered systems: Correlations and avalanches, *Spin Glass Theory and Far Beyond* (World Scientific, 2023), pp. 277–305.
[159] Edited by P. Charbonneau, E. Marinari, G. Parisi, F. Ricci-tersenghi, G. Sicuro, and F. Zamponi, *Spin Glass Theory and Far Beyond: Replica Symmetry Breaking after 40 Years* (World Scientific, 2023).
[160] N. Oyama, H. Mizuno, and A. Ikeda, Shear-induced criticality in glasses shares qualitative similarities with the Gardner phase, Soft Matter **19**, 6074 (2023).
[161] Y. Xing, Y. Yuan, H. Yuan, S. Zhang, Z. Zeng, X. Zheng, C. Xia, and Y. Wang, Origin of the critical state in sheared granular materials, Nat. Phys. **20**, 646 (2024).
[162] See Supplemental Material at http://link.aps.org/supplemental/10.1103/3rwf-d3yx for a movie showing the spatiotemporal dynamics and morphology of plastic avalanches in the postyield regime.
[163] S. Rossi, G. Biroli, M. Ozawa, G. Tarjus, and F. Zamponi, Finite-disorder critical point in the yielding transition of elastoplastic models, Phys. Rev. Lett. **129**, 228002 (2022).
[164] D. Fernández Castellanos, S. Roux, and S. Patinet, Insights from the quantitative calibration of an elasto-plastic model from a Lennard-Jones atomic glass, C. R. Phys. **22**, 135 (2021).
[165] P. Zhang, P. Cheng, J. Zhang, G. Liu, J. Weiss, and J. Sun, Coupled size and temperature effects on intermittent plasticity of BCC micro-crystals, Acta Mater. **260**, 119201 (2023).
[166] Y. Li, I. Lalani, M. Maron, W. Hixson, B. Wang, N. Ghoniem, and G. Po, Temperature-activated dislocation avalanches signaling brittle-to-ductile transition in BCC micropillars, Scr. Mater. **277**, 117233 (2026).